The upper mantle geoid for lithospheric structure and dynamics

F. Salajegheh[1], J.C. Afonso[2,3,1]

[1] Department of Earth and Environmental Sciences, Macquarie University, Sydney, Australia.
[2] Faculty of Geo-Information Science and Earth Observation (ITC), University of Twente, Enschede, Netherlands.
[3] Department of Earth and Space Sciences, Southern University of Science and Technology Shenzhen, Guangdong, China.

The upper mantle geoid for lithospheric structure and dynamics

F. Salajegheh[1], J.C. Afonso[2,3,1]

[1]Department of Earth and Environmental Sciences, Macquarie University, Sydney, Australia.
[2]Faculty of Geo-Information Science and Earth Observation (ITC), University of Twente, Enschede, Netherlands.
[3]Department of Earth and Space Sciences, Southern University of Science and Technology Shenzhen, Guangdong, China

Key Points:

- We present a new model of the upper mantle geoid to inform studies of the physical state of the lithosphere and sublithospheric upper mantle.
- We constrain the often ignored contributions of low degrees (< 8) in spherical harmonic expansions of the upper mantle geoid and clarify their geodynamic origin and impact on lithospheric studies.

Corresponding author: J. C. Afonso, `j.c.afonso@utwente.nl`

Abstract

Geoid anomalies offer crucial information on the internal density structure of the Earth, and thus, on its constitution and dynamic state. In order to interpret geoid undulations in terms of depth, magnitude and lateral extension of density anomalies in the lithosphere and upper mantle, the effects of lower mantle density anomalies need to be removed from the full geoid (thus obtaining a residual signal known as the 'upper mantle geoid'). However, how to achieve this seemingly simple filtering exercise has eluded consensus for decades in the solid Earth community. While there is wide agreement regarding the causative masses of degrees > 10 in spherical harmonic expansions of the upper mantle geoid, those contributing to degrees < 7-8 remain ambiguous. Here we use spherical harmonic analysis and recent tomography and density models from joint seismic-geodynamic inversions to derive a representative upper mantle geoid, including the contributions from low harmonic degrees. We show that the upper mantle geoid contains important contributions from degrees 5 and 6 and interpret the causative masses as arising from the coupling between the long-wavelength lithospheric structure and the sublithospheric upper mantle convection pattern, including subducted slabs. Importantly, the contributions from degrees $3 < l < 8$ do not show a simple power-law behaviour (e.g. Kaula's rule), which precludes the use of standard filtering techniques in the spectral domain. Our model of the upper mantle geoid will be useful in a wide range of geodynamic and geophysical applications, including the study of i) the thermochemical structure of the lithosphere, ii) dynamic topography and mantle viscosity, iii) the nature of the mechanical coupling of the lithosphere-asthenosphere system and iv) the global state of stress within the lithosphere and its associated hazards.

Plain Language Summary

Satellite measurements of the gravity field of the Earth constitute one of the most useful data sets to study the Earth's internal structure and its natural resources. A specific observation related to gravity is the so-called *geoid*. Historically, the geoid has played a critical role in the development of theories regarding the inner workings of the Earth, including plate tectonics and earthquake activity. However, using geoid observations to constrain the structure of the tectonic plates down to depths of around 350 km is plagued with technical difficulties. This steam from the fact that the geoid is not only sensitive to the structure of the tectonic plates, but to the density structure of the entire planet. Removing the undesirable effects associated with the Earth's deep structure to isolate the signal related to the shallower tectonic plates has been, and still is, an unresolved problem. In this study, we present a new model of the Earth's geoid that achieves exactly that, thus providing a new way to study the internal constitution and structure of tectonic plates and the location of critical natural resources.

1 Introduction

Geoid anomalies (or height) relative to a reference datum constitute one of the earliest and most useful data sets to make inferences about the Earth's internal density distribution and viscosity structure. With the advent of global tomography more than four decades ago, it was quickly recognized that the long-wavelength pattern of velocity anomalies in the deep mantle correlate with low-order expansions of the non-hydrostatic geoid (e.g., Hager & Richards, 1989; Hager et al., 1985; Ricard et al., 1989; Richards & Hager, 1984; Hager, 1984). Since such velocity anomalies were thought to be the result of planetary-scale convection, a number of geodynamic/global convection models were soon created to reconcile the long-wavelength patterns of both seismic velocities and geoid height (e.g., Liu & Zhong, 2015, 2016; Panasyuk & Hager, 2000b; Perrot et al., 1997). The success of these early global models cemented the idea that low-order undulations of the geoid are dominated by deep mantle density anomalies related to mantle flow. They also clarified the need for accounting for the flow-driven undulations of both the Earth's surface (dynamic topography) and internal surfaces across which large density contrasts exist (e.g. core-mantle boundary). Since these undulations would be absent in a non-convecting Earth, they are sometimes referred to as the 'dynamic' effect or contribution to the full geoid.

A much earlier but equally important realization that came out of pioneering studies of global gravity (see Chase, 1985) is the fact that neither gravity nor geoid anomalies can define their causative mass distribution uniquely. Spectral decompositions (spherical harmonic analysis, power spectrum) of the geoid offer additional insights, but they cannot remove completely the ambiguity in determining the depth vs. lateral extension of the causative density anomalies (i.e. is the anomaly deep or shallow and laterally extended?); all density anomalies inside the Earth contribute to all degrees and orders in a spherical or elliptical expansion of the geoid (cf. Liu & Zhong, 2015, 2016; Chase, 1985). This creates a significant problem when attempting to fit geoid observations with density models that consider only a portion of the planet (e.g. a finite domain of the upper mantle). In such cases, the effect of density anomalies outside the region of interest need to be either removed from the full geoid or accounted for during modelling; the former case is the most common in practice. A relevant example is the study of the structure and dynamics of the lithosphere-asthenosphere system using gravity/geoid data (e.g., Afonso et al., 2019; O'Donnell et al., 2011). Depending on the specific goals of the study, the contributions of either sublithospheric or lower mantle density anomalies need to be filtered out from the observed geoid in order to avoid the density model from being contaminated by the effect of deep (and unmodelled) density anomalies. Other 'classical' examples are the application of spectral analysis of the geoid (and topography) to determine possible differences in the convection patterns of the upper and lower mantle (e.g., Fleitout & Moriceau, 1992; Rong-Shan, 1989) and to constraint the viscosity structure of the mantle (e.g., Čížková et al., 1996; Panasyuk & Hager, 2000a; Kido et al., 1998; Čadek et al., 1998).

There are theoretical and empirical arguments that support the common conception that deep, large-scale density anomalies (e.g. undulations of the core-mantle boundary, ancient slabs in the lower mantle) contribute primarily to the low-order terms of a spherical harmonic expansion of the geoid, whereas shallower, smaller anomalies tend to contribute more significantly to the higher degrees and orders (Hager, 1984; Doin et al., 1996; Featherstone, 1997; Chase, 1985; Bowin, 1983, 2000; Chase et al., 2002; Golle et al., 2012; Coblentz et al., 2011). This ansatz has allowed a number of researchers to use different types of spectral filtering to remove (more precisely, minimize) the effect of deep density anomalies from the complete geoid when studying the shallow structure of the Earth. One of the most popular filtering approaches consists of removing a low-degree 'reference' geoid from the full geoid (e.g., McKenzie et al., 1980; Marks et al., 1991; Coblentz et al., 2015; Afonso et al., 2019; Fullea et al., 2021). This reference geoid is computed as a spherical expansion up to a certain threshold degree considered to represent a limit for contributions from deep, unmodelled density anomalies(Hager, 1984; Doin et al., 1996; Featherstone, 1997; Chase, 1985; Bowin, 1983, 2000; Chase et al., 2002; Golle et al., 2012; Coblentz et al., 2011). A slightly more sophisticated approach uses multitaper strategies to minimize undesirable artifacts that arise from sharp truncations of the harmonic expansion (e.g. Gibbs oscillations; (Afonso et al., 2019; Coblentz et al., 2015; Marks et al., 1991)).

The residual (filtered) geoid that results from removing the reference low-degree geoid is sometimes referred to as the 'upper mantle geoid' (e.g., Coblentz et al., 2015), as it is supposed to reflect primarily density anomalies in the upper mantle. Numerous works provided empirical evidence for removing degrees and orders below 8 - 11 when studying large-scale lithospheric structure and/or upper mantle features (cf. Afonso et al., 2019). For instance, in our previous study of global lithospheric structure (Afonso et al., 2019), we experimented with a number of filtering options and data sets and chose to remove orders and degrees < 8 and roll off (i.e. smoothly dampen) spherical harmonic coefficients between degrees 8 and 12 using a cosine taper function. In other words, wavelengths $> \sim 4700$ km were completely removed, those between 4700 km and 3200 km were rolled off, and those < 3200 km were preserved intact. Although such an approach is theoretically and empirically supported (see Supplementary material in Afonso et al. (2019)), and provides a practical solution for regional lithospheric studies, it is ultimately incorrect. Long-wavelength density anomalies that could contribute to orders and degrees < 8 are expected to exist above the mantle transition zone (e.g. continent-ocean distribution, hot-spots distribution, subducted slabs). However, their relative contributions to the residual geoid and their effects on density models of the lithosphere and upper mantle remain obscure. For instance, some authors have included the full contribution of lower degrees and orders (even down to degree 4) in their upper mantle geoid models (e.g. Chase et al. (2002); Coblentz et al. (2011); Afonso et al. (2019)). As mentioned above, although it is expected that orders and degrees $<$ 8-10 would contain a contribution from upper mantle density anomalies, including their full contributions (complete harmonic coefficients) in a harmonic expansion is unwarranted a priori and it would likely result in an overestimation of the size and magnitude of the causative density anomalies.

Although the spectral filtering approach has been the preferred option to obtain upper mantle geoid models, a more direct strategy (hereafter referred to as the 'direct approach') would be to compute the effect of all masses below the upper mantle (i.e. below 410 km depth) and remove it from the full non-hydrostatic geoid, thus obtaining the 'true' upper mantle geoid. The main difficulty with the direct approach is that it requires a reliable lower mantle density model, which traditionally have been difficult to obtain due to i) the relatively low resolution of earlier global tomography models used to convert velocities into density anomalies and ii) the uncertainties in the velocity-density conversion factors. Yet, the past decade has seen the generation of a number of high-resolution global models that warrant the reassessment of current practices for obtaining upper mantle geoid models and their geophysical-geodynamic implications. We note that a similar direct strategy was used by Hager (1984) to obtain his famous 'slab' residual geoid.

In this paper, we argue that the recent model of Lu et al. (2020) offers a plausible and practical choice for testing and applying the direct approach. The model created by these authors (henceforth referred to as SGM20) is based on the joint inversion of multiple geodynamic observations and an extensive dataset of seismic travel times for multiple phases and their surface bounce equivalents. It constitutes an important update from an earlier and similar global model (GYPSUM, Simmons et al. (2010)) and benefits from over two decades of continuous development. The SGM20 model also considers dynamic effects of deep mantle convection and uses improved, depth-dependent velocity-density scaling factors constrained by an exhaustive mineral physics database (Lu et al., 2020). In the following, we will use the lower mantle density structure (including the mantle transition zone) from SGM20 to obtain a range of representative models of the upper mantle geoid. In doing so, and making use of additional high-resolution upper mantle seismic models, we will put realistic constraints on the contributions from degrees and orders < 9 arising from upper mantle density anomalies. Our final residual geoid will be useful in studies assessing dynamic topography, crustal structure, lithospheric stresses, thermochemical structure of the lithosphere and basin analysis, to name a few.

2 The non-hydrostatic geoid

2.1 Synthesis and data

Here we work with the non-hydrostatic geoid rather than the more common 'geodetic' or true geoid. We do so because of two main reasons. First, being a measure of the

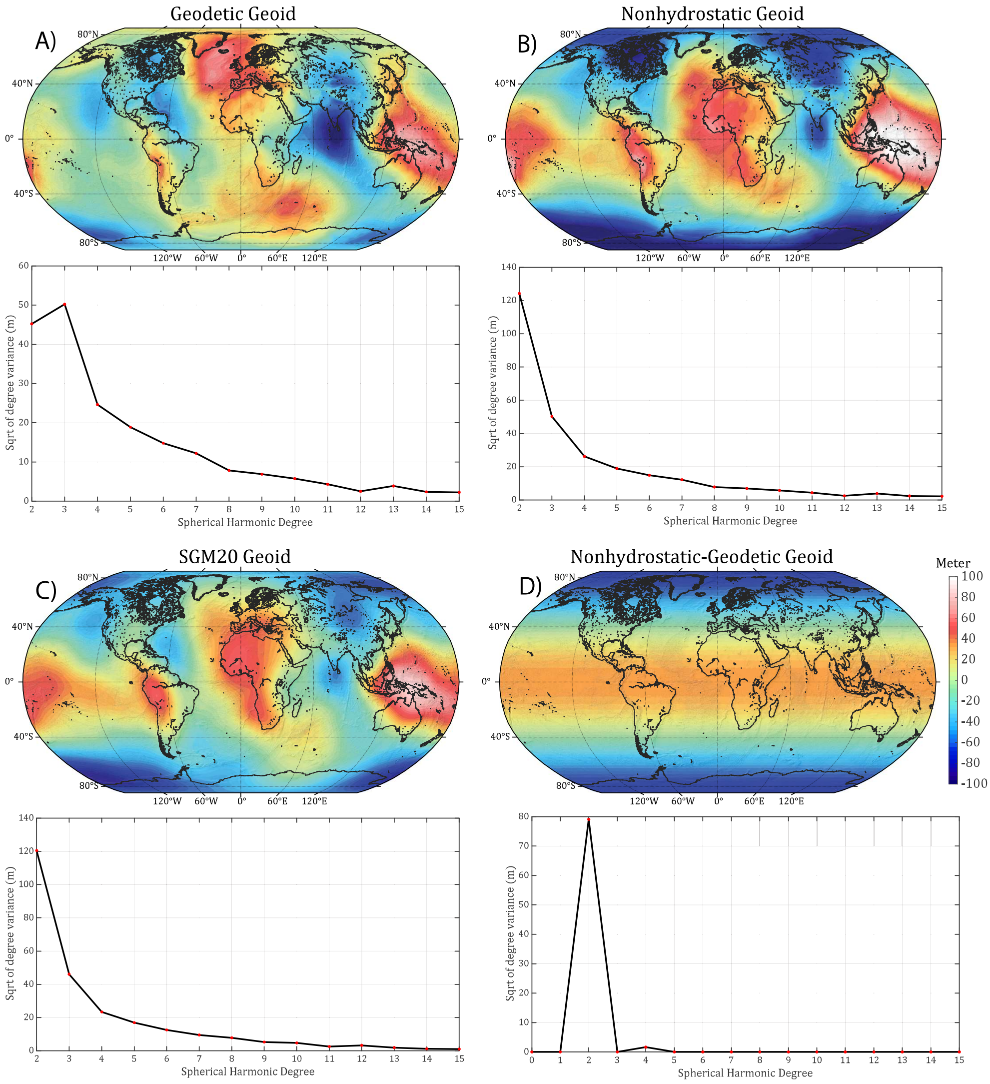

Figure 1. A) Observed geodetic geoid height and its power spectrum. B) Observed non-hydrostatic geoid height and its power spectrum . C) Geoid signal predicted by the lower mantle density structure (strictly, densities below 400 km depth) of the SGM20 model and its associated power spectrum. D) Difference between the non-hydrostatic and geodetic geoid and corresponding power spectrum.

deviations from hydrostatic conditions in a rotating fluid planet (Chambat et al., 2010; Nakiboglu, 1982), the non-hydrostatic geoid is easier to interpret in terms of geodynamic processes and the associated internal (re)distribution of masses. Second, for consistency with the SGM20 model, which was derived by fitting predictions to non-hydrostatic gravity anomalies explicitly considering viscous flow in a compressible self-gravitating mantle as well as the gravitational contributions of the deformation of the surface and the core-mantle boundary induced by dynamic stresses in the mantle. Regardless of our working choice, our non-hydrostatic upper mantle geoid can be easily converted into its geodetic equivalent by changing the reference (in practice, one needs only to change the spherical harmonic coefficients C_{20} and C_{40} in the expansion; see below).

We expand the Earth's gravitational potential in spherical harmonics as:

$$\begin{aligned} N &= \frac{GM}{r\gamma} \sum_{l=2}^{lmax} \left(\frac{a}{r}\right)^l \sum_{m=0}^{l} f_{lm} P_{lm}(\cos\phi) \\ f_{lm} &= (C_{lm}\cos m\lambda + S_{lm}\sin m\lambda) \end{aligned} \tag{1}$$

Where N is the observed geoid anomaly at a point on the Earth's surface located at latitude ϕ, longitude λ and radius r; G is the gravitational constant, M the Earth's total mass, γ the normal gravity at the Earth's surface, a the semi-major axis of the reference ellipsoid, C_{lm} and S_{lm} are fully normalized coefficients of the spherical harmonic expansion, $P_{lm}(cos\phi)$ are fully normalized associated Legendre functions and n and m are the degree and order of the expansion, respectively. For a sphere of radius R, each spherical harmonic degree l has an equivalent wavelength λ on the surface of the sphere, given by the Jeans relation, $\lambda = 2\pi\mathrm{R}/l(l+1) \approx 2\pi\mathrm{R}/(l+1/2)$. All spherical harmonic syntheses and analyses in this work are performed with a modified version of the code described in Wang et al. (2006).

The observed geoid data is taken from the Earth Gravitational Model 2008, which includes degrees and orders up to 2159, with additional coefficients up to degree 2190 and order 2159 (Pavlis et al., 2012). In order to compute non-hydrostatic geoid anomalies (i.e. geoid undulations referred to the equilibrium hydrostatic ellipsoid), we replace the spherical harmonic coefficients C_{20} and C_{40} in Eq. 1 with those computed by Chambat et al. (2010). Figure 1 shows a comparison between the geodetic and the non-hydrostatic geoid. As mentioned before, the difference between the two is only significant for even degrees 2 and 4 and order 0 (Chambat et al., 2010), with $|C_{20}|$ being ~ 486 times larger than $|C_{40}|$.

2.2 Power spectrum and degree correlation

Since the full spectrum analysis of a modern geoid model involves many harmonics, here we adopt the common practice of summarizing the power spectrum of the geoid by the combined amplitudes of all orders ($0 \leq m \leq l$) for each degree l:

$$\sigma_l^2 = \sum_{m=0}^{l} \left[(C_{lm})^2 + (S_{lm})^2 \right] \tag{2}$$

where σ_l^2 is so-called degree variance; its square root is often used to denote the variation of the amplitude spectrum, which indicates the relative power of each wavelength (degree) to the total signal.

A related and useful concept that we will use below is that of the *degree-correlation* function, which is a measure of per-degree similarity between two spherical harmonic expansions (e.g. different geoid models in the present context; e.g., Kaula (1967); O'Connell (1971); Lambeck (1976); Cazenave et al. (1986); Wieczorek (2007); Forte et al. (2010)). For a given harmonic degree l, the correlation coefficient between two potential fields A and B is

$$D_l(A,B) = \frac{\sum_{m=0}^{l}(C_{lm}^{A}C_{lm}^{B} + S_{lm}^{A}S_{lm}^{B})}{\sigma_l^A\sigma_l^B} \tag{3}$$

where C_{lm}^{A}, C_{lm}^{B}, S_{lm}^{A} and S_{lm}^{B}, are the spherical harmonic coefficients and σ_l^A and σ_l^B the square roots of the respective degree variances. The correlation coefficient is dimensionless, and satisfies the relation $-1 \leq \mathrm{D}_l \leq +1$.

Figure 1 shows the power spectrum of the full non-hydrostatic geoid, displaying the typical power-law rule of the form $\sigma_l^2 \sim (2l{+}1)(10^{-5}l^{-2})^2$ (Kaula's Rule; Kaula (1967)). The power spectrum is clearly dominated by degrees 2-4, which amount to more than 64% of the geoid signal. It is now well-known that degrees 2 and 3 are predominantly generated by flow-related anomalies in the deep mantle (Bowin, 1983, 2000; Hager & Richards, 1989; Hager et al., 1985; Ricard et al., 1989; Richards & Hager, 1984; Hager, 1984; Liu & Zhong, 2015, 2016) and therefore models of the upper mantle geoid should have a negligible power associated with these degrees. Indeed, when we look at the square root of the degree variance and degree correlation predicted by the lower mantle contribution of the SGM20 model, we see that the great majority of the full geoid signal at degrees 2 and 3 is explained by the density field at depths > 400 km (Fig. 1). In other words, the relative difference in the predicted and observed σ_l^2 is small (i.e. the power of the SGM20 'lower mantle' geoid is similar to that of the full observed geoid) and $D_l(obs, SGM20)$ is high (i.e. the spatial pattern of the SGM20 'lower mantle' geoid is similar to that of the full observed geoid; Suppl. Figs. S3 and S7). These observations suggest plausible dual criteria for obtaining a residual upper mantle geoid and representative contributions of all relevant degrees and orders. We describe these criteria in the next section.

3 The residual upper mantle geoid

We begin by generating a preliminary residual geoid, hereafter referred to as UMG1, by subtracting the SGM20 'lower mantle' contribution from the full, observed non-hydrostatic geoid. By 'SGM20 lower mantle contribution' we mean the signal predicted by the SGM20 density structure at depths > 400 km, including the effects of viscous flow, compressibility, self-gravitation and core-mantle boundary ellipticity (Lu et al., 2020). The UMG1 model is a continuous function $f(\lambda, \phi)$ over the Earth's surface and therefore it can also be expanded in spherical harmonics (Fig. S1A).

Since degrees 2 and 3 are dominated by density heterogeneities well below the upper mantle (e.g., Hager & Richards, 1989; Hager et al., 1985; Ricard et al., 1989; Richards & Hager, 1984; Hager, 1984; Liu & Zhong, 2015, 2016), we can confidently remove any residual contribution from these degrees from UMG1 without loss of generality or accuracy. The case for *orders* 2 and 3 is less straightforward due to their dependence on latitude. Degrees $l > 3$ in the spherical harmonic expansion can also contain a significant contribution from their associated orders 2 and 3 (i.e. terms C_{43}, C_{42}, etc). This is indeed the case, as shown in Suppl. Fig. S1B. At low latitudes, these contributions represent very long-wavelengths linked to deep anomalies and therefore they should be also removed from the expansion. Conversely, the same orders at high latitudes are associated with much shorter wavelengths, and they likely contain a considerable contribution from shallow density anomalies. We therefore apply a latitude-dependent filter to orders 2 and 3 of degrees 4-11 (the effect for degrees higher than ~ 10 is negligible).

$$f_{lm}^{'} = f_{lm} - w(\phi)f_{lm}\Big|_{m=1,2}^{l=4...11} \tag{4}$$

where f'_{lm} is filtered form of f_{lm} in equation 1 and $w(\phi)$ has the form

$$w(\phi) = \left[\frac{r}{D_{equ}} \times \arctan\left(\frac{\sqrt{(\cos\phi \cdot \sin(\Delta\lambda))^2 + (\cos\phi \cdot \sin\phi - \sin\phi \cdot \cos\phi \cdot \cos(\Delta\lambda))^2}}{\sin\phi \cdot \sin\phi + \cos\phi \cdot \cos\phi \cdot \cos(\Delta\lambda)} \right) \right]^{\alpha} \tag{5}$$

where $0 \leq w(\phi) \leq 1$, ϕ is latitude in radians, r is the Earth's radius, D_{equ} is the length of a degree of longitude at the equator ($D_{equ} \simeq 111.17$ Km when ϕ=0) and $\Delta\lambda$ is a constant equivalent to a degree of longitude in radians ($\Delta\lambda = \pi/180$). The effect of α on the shape of the filter is shown in Suppl. Fig. S2. Higher values of α produce a more rapid decay of the orders 2-3 with latitude. The resulting residual upper mantle geoid, referred to as UMG2, is shown in Fig. 3A.

Summarizing, what we have done so far is i) to remove the lower mantle contribution from the full non-hydrostatic geoid using the density structure of model SGM20 (UMG1) and ii) filter out degrees 2 and 3 from the residual UMG1 model as well as orders 2 and 3 with a latitude-dependent filter (obtaining the UMG2 model). The pattern of highs and lows in UMG2 resembles surface tectonic features much closer than either the full geoid (Fig. 3A) or UMG1 (Fig. S1A). However, its power is dominated by the low degrees 4-7 and peak-to-peak geoid amplitudes between MORs and abyssal plains along corridors of oceanic lithosphere that have not been affected by plume activity are around twice as large as those predicted by models of lithospheric cooling (cf. Haxby and Turcotte (1978); Sandwell and Schubert (1980); Marquart (1991); Doin and Fleitout (1996); Sandwell (2022)). Also, the asymmetric nature of the low harmonic terms of order 0 is exceedingly large, resulting in large positive anomalies around the arctic circle and large negative ones around the south pole. We also note that the geoid variation across the Arctic basin and the northern Russian platform is also much larger than that expected from its isostatic state and lithospheric structure (Lebedeva-Ivanova et al., 2019; Pease et al., 2014; Ji et al., 2021).

These observations are not surprising given i) the fact that the amplitudes of the harmonic coefficients increase exponentially as we move towards low degrees/orders (Kaula's rule) and ii) that the power spectrum is a function of the absolute amplitudes of the harmonic coefficients (eq. 2). This means that even though the SGM20 'lower mantle' contribution explains well the low degrees of the total geoid (Fig. 1), any small misfit is in fact disproportionately large in absolute value when compared to the contributions from higher degrees. This scaling issue can be easily removed (or at least, largely minimized) by working with relative contributions per degree.

Given the complex joint inversion used to create model SGM20, we do not have a straightforward and rigorous way of assessing how much of the absolute magnitude of the upper mantle signal is contaminating the lower mantle structure of SGM20 (and vice versa) or the quality of fit for data sensitive to the lower mantle. However, we can get useful additional information on relative contributions from comparing the degree correlation between the lower mantle geoid from SGM20 and the full geoid for each degree. Borrowing from the observations in Section 2.2, the main idea is that the greater the similarity of spatial patterns between the lower mantle geoid and the real geoid for specific degrees, the greater the relative contribution from deeper sources to those degrees in the full geoid. For instance, if the correlation for degree l between the full geoid and the lower mantle geoid is 100%, we can assume that most of the power of degree l is explained by the lower mantle density structure (plus other dynamic effects accounted for by the SGM20 model). By the same token, a low correlation for degree l means that there is a small relative contribution of structures deeper than 400 km to the power associated with that degree.

Although valid and instructive as an analysis tool, this comparison is semi-quantitative at best given the potential uncertainties in the original SGM20 model and the natural ambiguity of spherical harmonics treatments of potential field data. With this caveat, we use the above idea to define a correction factor per degree to better estimate the *relative* contributions from deep vs shallow density anomalies to the power spectrum. This factor has the form

$$\mathrm{R}_l = 100 \times [1 + \beta D_l(geoid, SGM20)]/(1+\beta) \tag{6}$$

Where $D_l(geoid, SGM20)$ is the degree correlation coefficient defined in Eq. 3, between non-hydrostatic geoid and SGM20 (see Suppl. Fig. S3), and β is a weighting factor. With this definition, R_l is non-dimensional and tends to a minimum when β is increased (see figure 2), indicating that degree l is dominated by density anomalies above 400 km depth. We calibrated β so as to produce peak-to-peak geoid variations between MORs and unperturbed old oceanic lithosphere of the same order as those predicted by cooling models of oceanic lithosphere (cf. Haxby and Turcotte (1978); Sandwell and Schubert (1980); Marquart (1991); Doin and Fleitout (1996); see also Fig. 9C). We only apply this scaling for degrees <10, as its effect is negligible for degrees > 10-11 (i.e. the effects of deep density anomalies are small at these degrees, e.g. Lu et al., 2020). We corroborated the latter assumption by testing the effects of changing the cut-off degree (and thus the value of β) from 9 to 15. We have also computed the complement to the above correlation, namely the degree correlation per degree of two recent *upper mantle* geoid models (see Suppl. Material, Fig. S4) and confirmed that, as expected, the correlations tend to increase steadily with degree (i.e. the upper mantle density models explain higher degrees increasingly better).

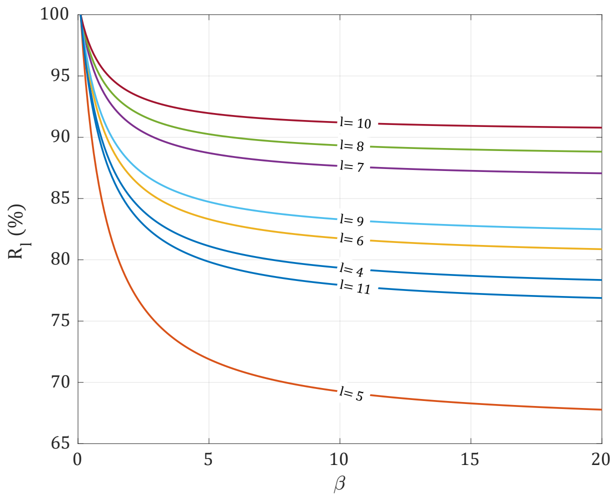

Figure 2. Variation of factor R_l versus weighting factor β (See Eq. 6)

The anomaly pattern of the final upper mantle residual geoid (i.e. after applying corrections 5 and 7), hereafter referred to as UMG3, is shown in Fig. 3B together with its power spectrum. The spatial pattern of anomalies of UMG3 correlates exceedingly well with major surface tectonic and topographic features, such as mid-ocean ridges (MORs), orogenic plateaus and large sedimentary basins in low-lands. As expected, peak-to-peak geoid variation between MORs and abyssal plains along corridors of oceanic lithosphere that have not been affected by plume activity is now within the predicted range from plate cooling models. Compared to the power from degrees >= 10, the power spectrum of UMG3 shows only a small contribution from degree 4, modest power contributions from degrees 7-9, and a considerable contribution from degrees 5 and 6 (especially the term of degree 5 and order 0; see Suppl. Material Fig. S1).

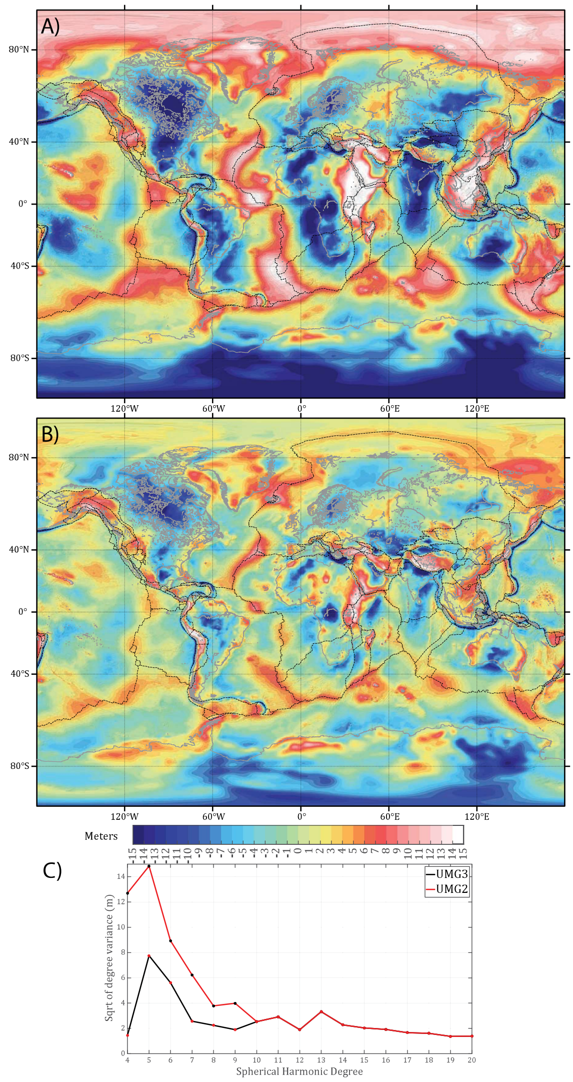

Figure 3. A) The residual model UMG2, obtained by filtering out degrees 2 and 3 and orders 2 and 3 (with a latitude-dependent filter) from model UGM1. B) The final 'upper mantle' geoid model UMG3. D) Power spectra of models UMG3 (black line) and UMG2 (red line).

Figure 4B shows the spectrum of the degree correlation of UMG3 with topography. For comparison, we also plot the spectrum of the full non-hydrostatic geoid. We see that while no coherent correlation exists for low orders in the full geoid, there is a consistent positive correlation for degrees >6-7. This observation has been long known (e.g. Kaula (1967); Toksöz et al. (1969); Lambeck (1976)) and it applies to both isostatically-corrected and raw topography. Based on comparisons between isostatic models of the gravity potential and the real geoid, Lambeck (1976, 1979); Rapp (1982a), among others, concluded that this positive correlation between the full geoid and surface topography can be attributed to shallow density anomalies (including the topography itself) that are close to isostatic equilibrium, rather than to dynamic density anomalies deeper in the mantle (note that these comparisons were made for crustal compensation mechanisms only). Similar conclusions were also put forward by other authors (e.g. McKenzie (1966); Kaula (1967)). As seen in Fig. 4, the pattern of correlation for both the full geoid and the UMG3 model are somewhat similar. Indeed, the powers for degrees >10 remain close, supporting the well-known view that lower mantle structure does not significantly affect topography or its compensation at degrees > 10-11. On the other hand, the positive correlations associated with the full geoid for degrees 6-10 have lost power in the case of the upper mantle geoid. The reason behind this observation is difficult to constraint unequivocally, but the patterns in Figs. 3 and Supplementary Fig. S5 and S6 do indicate that at least some of the anomalies below 400 km depth in the SGM20 model contribute to topography at these degrees. We discuss this further in Section 4.2.

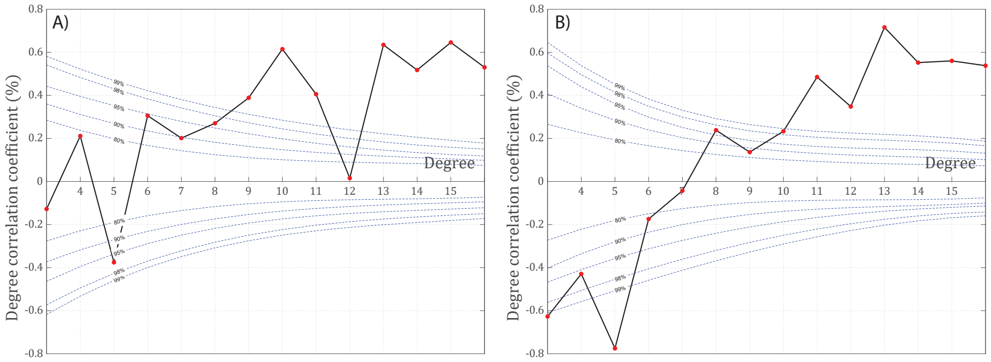

Figure 4. A) Correlation coefficients between topography and non-hydrostatic geoid for individual degrees B) Same as A) but for model UMG3. Dashed blue contours illustrate confidence levels of 99%, 98%, 95%, 90% and 80% (a confidence level of 95% indicates a 5% probability that the observed correlation is random).

There is also a strong negative correlation between the geoid and topography at degree 5 (Fig. 4); this is true for both the full (see also Lambeck (1976); Rapp (1982b)) and the residual upper mantle geoid. The strong power of degree 5 in both power spectra clearly points to the presence of density anomalies in the first 400 km with dominant half-wavelengths $\lambda/2 \sim$ 3000-4400 km. The fact that the degree correlation between the UMG3 model and topography is strongly negative while that for degrees > 6-7 is consistently and increasingly positive is also indicative of different processes operating in the upper mantle at these wavelengths and contributing differently to the geoid signal. In this context, it is interesting to note that the power spectrum of the Earth's topography has high and similar powers at degrees 4 and 5, after which there is a marked break in the slope of the spectrum (Fig. 5). The power of higher degrees decay quickly after degree 5, following a typical power law. These observations and the nature of degrees 5 and 6 in the power spectrum of upper mantle geoid models have been hardly identified or addressed in previous studies. We return to this observation in Section 4.2.

4 Discussion

4.1 Comparison with previous models

Figure 6 shows a comparison between our new residual geoid (UMG3) and three other models of the upper mantle geoid. Fullea et al. (2021) removed the contributions from degrees 2 and 3 from the full geoid in their study of upper mantle structure, leaving the full contributions of harmonic terms =>4. Although these authors also tested the effects of truncating the geoid at degree 9 (see their Appendix C), their results and interpretations were based on the geodetic geoid sharply truncated at degree and order 4. Our previous analysis suggests that preserving the full (degrees and orders) contribution of harmonic terms $3 < l < 8$, which dominate the power spectrum of their filtered geoid model (see Fig. 6) and are likely related to deep anomalies, remains unwarranted

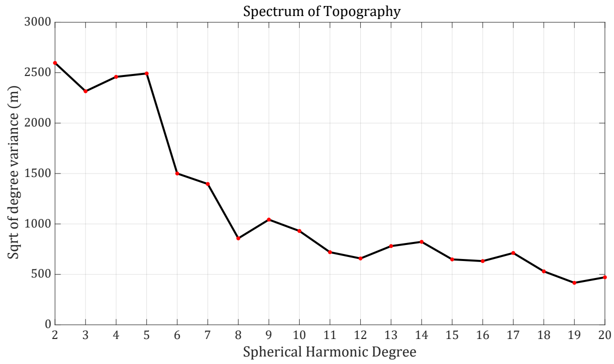

Figure 5. Square root of degree variance of the Earth's global topography.

and could result in considerable and undesirable artifacts in the derived density structure of the lithosphere.

The upper mantle geoid of Coblentz et al. (2015) was generated by removing spherical harmonic terms of degree/order < 6 and > 355; a cosine taper was applied to terms between degrees 6 and 9. This approach is similar to that used by Chase et al. (2002), who presented a similar upper mantle geoid model in their study of the Colorado Plateau (we do not show this geoid model as it is almost identical to that of Coblentz et al. (2015)). The only difference is that the latter authors preferred to remove harmonic terms < 7, therefore their upper mantle geoid exhibits somewhat lower amplitudes.

The upper mantle geoid of Afonso et al. (2019) was obtained based on a hybrid empirical-theoretical approach that involved i) a detailed analysis of the contributions of density anomalies of different sizes and at different depths to each harmonic degree of the geoid and ii) multiple inversions of real data filtered at different degrees. These authors concluded that removing orders and degrees < 8 and rolling off spherical harmonic coefficients between degrees 8 and 12 using a cosine taper function provided the best compromise. However, recognising that the effect of mass anomalies below 400 km was non-negligible on a filtered geoid up to degree and order ~ 10, they also estimated possible contributions from deep anomalies using a global tomography model (Panning & Romanowicz, 2006) and removed them from their filtered geoid.

Given the differences and/or similarities in the above approaches, it is not surprising that the UMG3 model is most similar to that of Coblentz et al. (2015) and Afonso et al. (2019). Compared to the model of Coblentz et al. (2015), UMG3 exhibits overall smaller amplitudes. As explained further below, this is mainly a consequence of the large residual contributions from degrees 7 and 8 in the model of Coblentz et al. (2015). A closer inspection reveals some significant differences, e.g. in eastern China, in India and its oceanic surroundings and around the Reykjanes ridge. The pattern in the UMG3 model seems to be in closer agreement with the abundant seismic and geochemical evidence of lithospheric mantle erosion and upper mantle upwellings in eastern China (e.g., Zhang et al., 2009). Likewise, recent tomography and gravity models in the North Atlantic do not seem to indicate large asymmetries in the upper mantle (i.e. above 400 km) across the Reykjanes ridge (Delorey et al., 2007; Celli et al., 2021; Minakov & Gaina, 2021) which would induce the strong asymmetric anomalies observed in Fig. 6D (although such anomalies may exist in the transition zone and uppermost lower mantle; e.g. Celli et al. (2021)). The differences in India are somewhat more puzzling. The model of Coblentz et al. (2015) preserves a much stronger negative geoid signal coinciding precisely with the location of the controversial Indian Ocean Geoid Low (IOGL), the largest negative anomaly in the full geoid. This large low in their upper mantle geoid affects (decrease) the values

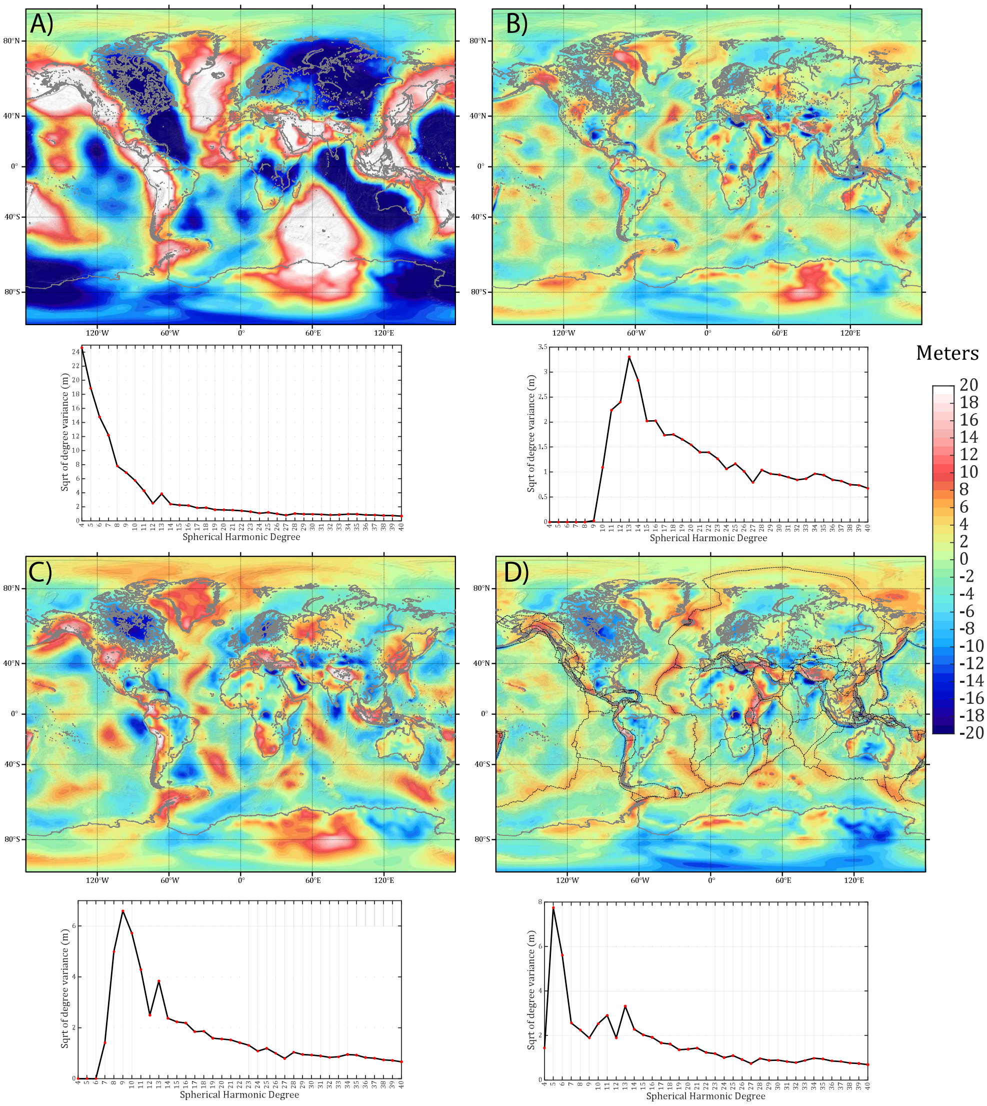

Figure 6. A comparison between UMG3 and three other models of the upper mantle geoid. A) WINTERC (Fullea et al., 2021), B) $LithoRef18$ (Afonso et al., 2019), C) the model of (Coblentz et al., 2015), D) UMG3.

in the adjacent continental lithosphere as well, which also shows negative values. This is somewhat unexpected given the surface topography across the ocean-continent transition in southern India. An inspection of the individual contributions of each degree (Suppl. Material; Fig. S7) reveals that degrees 3, 5, 6, 8 and 9 contribute significantly to the low values of the IOGL. Degrees 3 and 8, in particular, contain most of the power. Since the filtering strategy of Coblentz et al. (2015) results in a residual geoid with a large contribution from degree 8 (Fig. 6), it is not surprising that the IOGL is more prominent in their model. This also applies to other anomalies with a strong contribution from degree 8 (e.g. the low between Mozambique and Madagascar, the extreme high-low pairs in the Nazca plate and between the eastern Aleutian trench and the north Pacific plate; see Fig. S7 in Suppl. Material).

The similarity between the UMG3 model and that of Afonso et al. (2019) is striking, although the present model shows a clearer correlation with known surface features in the ocean (particularly in the Pacific), a slightly larger peak-to-peak amplitude between MORs and undisturbed abyssal plains and stronger negative amplitudes over north-America. The asymmetric nature of the harmonic term of degree 5, order 0 is also more evident in the UMG3 model, with broad but small positive anomalies in the Arctic region and negative anomalies around the south pole. We emphasize that the close agreement between these two models is far from coercive and it should not be taken lightly. These two upper mantle geoid models have been obtained from different sources (e.g. different tomography/lower mantle models), following considerably different approaches (filtering/hybrid vs direct). The fact that these two approaches converged to similar models is encouraging and adds confidence to the representativeness of the present model. In the next section, we discuss additional evidence in support of our results.

4.2 Contribution from low degrees to the upper mantle geoid

We have pointed out in the previous section that the upper mantle geoid contains only modest contributions from harmonic degrees 4, 7 and 8, and a considerable contribution from harmonic degrees 5 and 6 (Fig. 6D). This indicates that significant density anomalies with half-wavelengths $\lambda/2 \sim 3000$-4400 km may exist in the upper 400 km of the Earth. If this is true, we should expect to see a similar pattern of seismic anomalies in modern global tomography models of the upper mantle (under the reasonable assumption that a sizable fraction of both density and velocity anomalies are controlled by the same physical variable, namely temperature). By implication, a strong correlation between the upper mantle geoid and tomography models at degree 5 is also expected.

We plot the anomaly patterns of both our residual upper mantle geoid and those from a recent shear-wave tomography model (Schaeffer & Lebedev, 2013) at four different depth intervals in Figure 7. The power spectrum of the degree correlation between these two models is depicted in fig. 8; their per-degree expansions are shown in Suppl. Fig. S8. It is immediately apparent from these figures that there is a strong degree 5 component in the velocity anomalies at depths from 80 to 350 km. The component related to degree 6 is also prominent in the depth range 80-300. In this latter depth interval, the correlation coefficients between the SL2013 model and UMG3 range between 0.7-0.9 and 0.55-0.75 for degrees 5 and 6, respectively (Fig. 8). As expected, the power of the degree correlation tends to decrease more or less steadily with degree and depth for degrees > 11-13. In other words, the higher the degree or the deeper the slice of seismic anomalies, the smaller the correlation between the two fields. Other recent seismic models of the upper 400 km of the Earth (French & Romanowicz, 2014; Pasyanos et al., 2014; Simmons et al., 2010; Fichtner et al., 2018), including the upper mantle component of SGM20, show similar power spectra and degree correlations (not shown here).

It seems clear, therefore, that the contributions of degrees 5 and 6 to the upper mantle geoid obtained in Section 3 are not artifacts, but a real effect arising from the thermal-density structure of the first ~ 350 km, including slabs (cf. Cazenave et al. (1989)). Indeed, the degree 5 pattern of the SL2013 tomography model in the depth range 80-200 km shows positive (fast) seismic anomalies located near regions where old oceanic lithosphere and thick continental lithospheric roots are known to exist (e.g. North America,

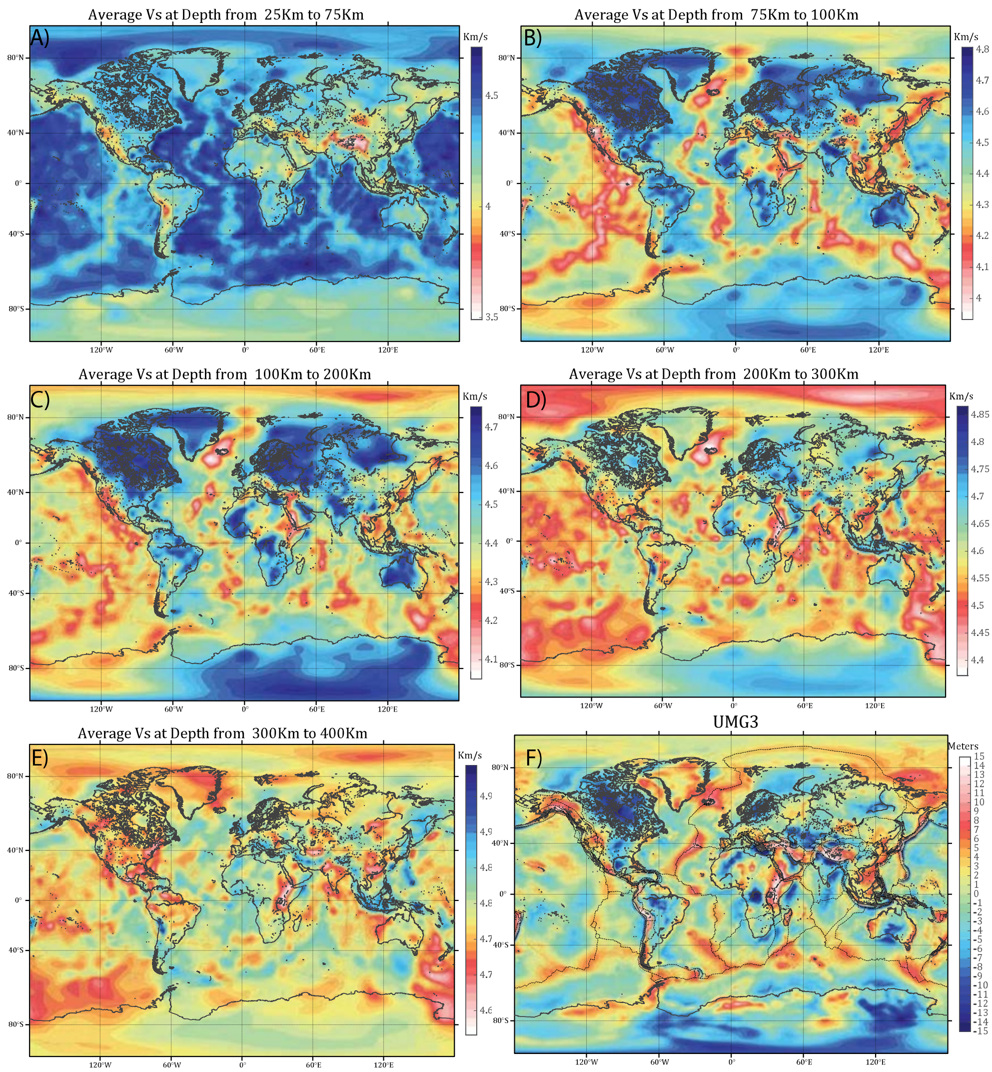

Figure 7. A-E) depth-averaged velocities from model SL2013 for different depth intervals. F) UMG3 model.

Western Australia, West African Craton, western Pacific; Fig. S8). In contrast, the strongest negative (slow) anomalies tend to be located near regions where upper mantle upwellings have been inferred either from joint geodynamic-geophysical inversions (e.g. Rowley et al. (2016); Schubert (2015); Forte et al. (2010)), from stratigraphic records (Hoggard et al., 2016; Flament et al., 2013; Rowley et al., 2013; Moucha et al., 2008) or from the location of MORs and rifts/hot-spots (e.g. Afar, Tristan Da Cuhna; Figs. 6D and S8).

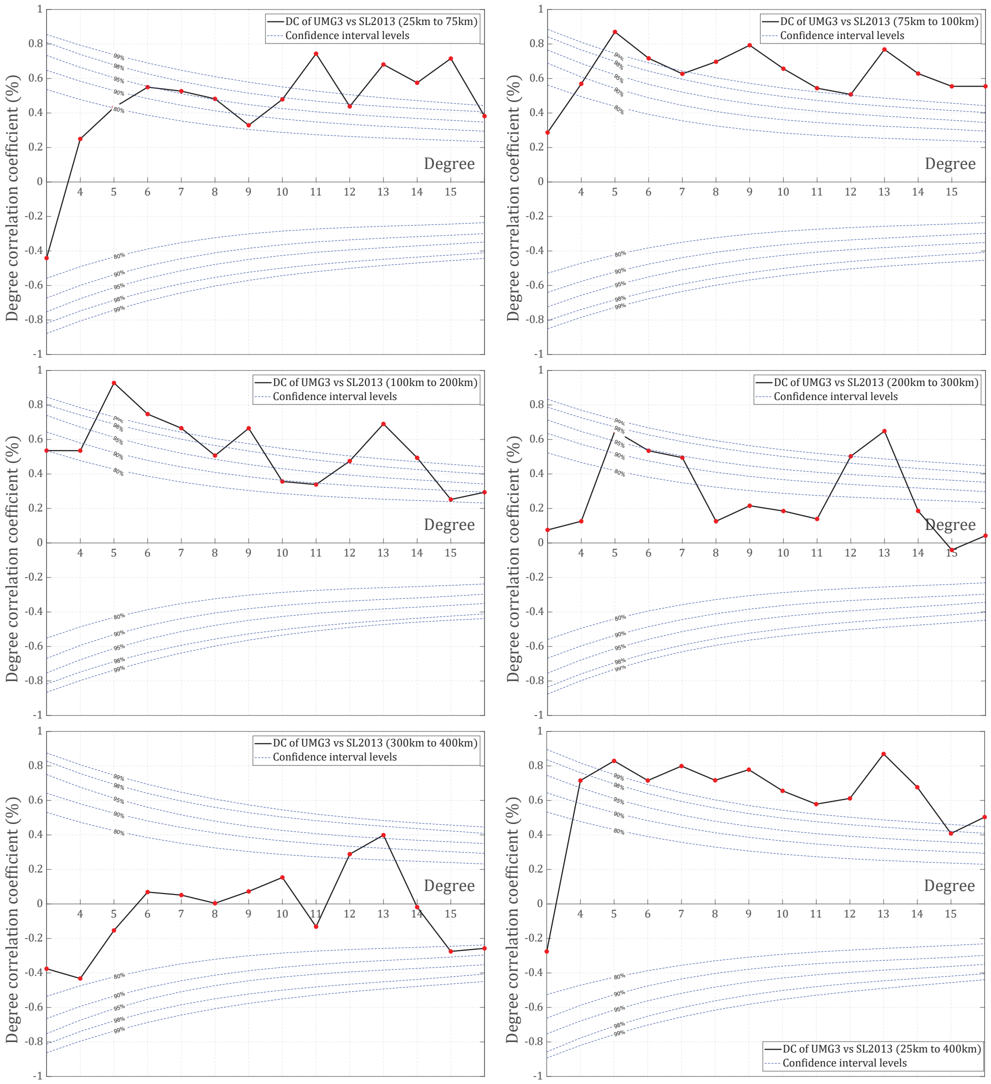

Figure 8. Per-degree correlation coefficients between the UGM3 model and the SL2013 seismic velocity model at different depth intervals. Dashed blue lines indicate the confidence levels of 99%, 98%, 95%, 90% and 80%.

The point raised above bears implications for another curious observation made in Section 3 regarding the correlation between topography and upper mantle geoid. We have already shown that the full geoid shows a consistent positive correlation with topography for harmonic degrees 6 and above (Fig. 4). The residual upper mantle geoid UGM3 exhibits a similar pattern, but the positive correlation becomes clearer for degrees > 7, with degrees 6 and 7 showing a poor correlation. In both cases (full and upper mantle geoid), however, degree 5 shows a strong and negative correlation. If we accept the common view that the positive correlation for higher degrees is related to (mostly) isostatically compensated near-surface density anomalies of equivalent half-wavelengths $\lambda/2$ $\sim$ 3000-2000 km (e.g. Lambeck (1976, 1979); Rapp (1973); Cazenave et al. (1992), and to non-compensated short-wavelength topographic features (Le Stunff & Ricard, 1995), then the mechanism responsible for a strong negative correlation between geoid and topography has to be equivalent to a downward pull of positive topography or an upward push of negative topography (i.e. overcompensation). Such effect is precisely what dynamic effects related to convection flow in the sublithospheric mantle would produce. Forte et al. (1993) was among the first to use seismic tomography and mantle flow models to suggest that some long-wavelength gravity lows in cratonic areas were the result of downgoing flow associated with a dense and thick lithosphere. Although the absolute magnitude of this effect is highly contentious (cf. Panasyuk and Hager (2000a); Le Stunff and Ricard (1995); Flament et al. (2013); Davies et al. (2019)), deep lithospheric roots do tend to either nucleate or force downwellings in a convecting mantle that can exert a 'suction effect' over long wavelengths; this depresses surface topography and decreases the geoid signal. Similarly, upwellings are focused in regions of thin lithosphere and can produce surface topography to bulge, which in turn increases the geoid signal. We note that the actual dynamic effect on topography does not have to be large to produce considerable changes in the geoid. This is because the air/water to rock density contrast is large and close to the surface; a modest depression of continents with positive topography and close to isopicnicity (Jordan, 1978) can result in a significant geoid reduction. This concept is also in agreement with other recent models of present-day sublithospheric mantle flow (Bredow et al., 2022; Simmons et al., 2010; Rowley et al., 2016; Lu et al., 2020). In this context, we note that the recent estimate of global dynamic topography by Davies et al. (2019), in which lithospheric structure was accounted for, shows considerable power at degrees 5 and 6.

There is one more observation of relevance to our discussion, namely the power spectrum of topography itself (Fig. 5). As mentioned in Section 3, there is a sharp break in the slope of the spectrum at degree 5. The lack of correlation between full geoid and topography at degrees $2< l < 5$ is commonly attributed to the continental masses (Cazenave, 1995), which contribute significantly to the power of topography but induce negligible effects to the geoid due to their general state of isostatic equilibrium. This supports the well-known anstaz that long-wavelength geoid undulations are mostly related to deep density anomalies of dynamic origin (Richards et al., 1988; Hager, 1984; Hager & Richards, 1989; Hager et al., 1985). Similar to the power-law behaviour of the geoid's spectrum, the power spectrum of topography for harmonic degrees > 6 also follows a power-law, commonly referred to as the Vening Meinesz rule (Vening Meinesz, 1951). However, it is not obvious from the power spectrum alone whether degree 5 is part of the 'normal' power-law behaviour or part of the 'dynamic' trend that characterizes low degrees. The analysis and interpretation given above regarding the nature of the causative anomalies contributing to degree 5 of the upper mantle geoid favour the view that the break at degree 5 in the topography spectrum represents a 'transition' between these two main states of compensation (i.e. degree 5 contains a mixed contribution from dynamic and isostatically compensated density anomalies). In this regard, we note that the classic 'slab geoid model' of Hager (1984) and its alleged contributions to degrees 4 to 9 where derived from a relatively simple slab model with no consideration of lithospheric structure. Given that we have established the critical role of lithospheric structure to the power and degree correlation of degrees 5 and 6 in the residual upper mantle geoid, the common interpretation of a 'purely slab component' for degree 5 is likely incorrect; at the very least both effects (i.e. slabs in the upper mantle and lithospheric structure) are intermingled in the upper mantle geoid signal. However, the precise quantification of which process dominates (if any) the power of degree 5 remains elusive and beyond the scope of this paper.

4.3 Uncertainties in the final geoid model

At present, there are no available uncertainty estimates associated with the SGM20 density model. Although this precludes us from performing a formal error propagation analysis, we can attempt to identify the main sources of uncertainty in the SGM20 model and use these in conjunction with potential uncertainty sources in our approach to obtain a practical estimate of the uncertainties in our final geoid model.

Of the many factors that can contribute to the final uncertainty of the SGM20 density model, the four dominant ones are i) the irregular coverage of the seismic data (and associated lack of resolution of the tomography problem), ii) the linearization of the problem, iii) the regularization (smoothing) imposed during the joint inversion and iv) the scaling factor to convert velocity anomalies to density anomalies. Using estimates from other similar tomography models and recent studies on uncertainty estimates (Becker & Boschi, 2002; Van Camp et al., 2019; Auer et al., 2014), we can pose a minimum uncertainty for the lower mantle velocity model of no less than 2-4%.

With respect to point iv) above, Lu et al. (2020) provided comprehensive estimates of the uncertainty affecting the scaling factor ρ/Vs used to convert velocities to densities. Based on their analysis, we can assign a generous uncertainty of ± 0.085 to the scaling factor.

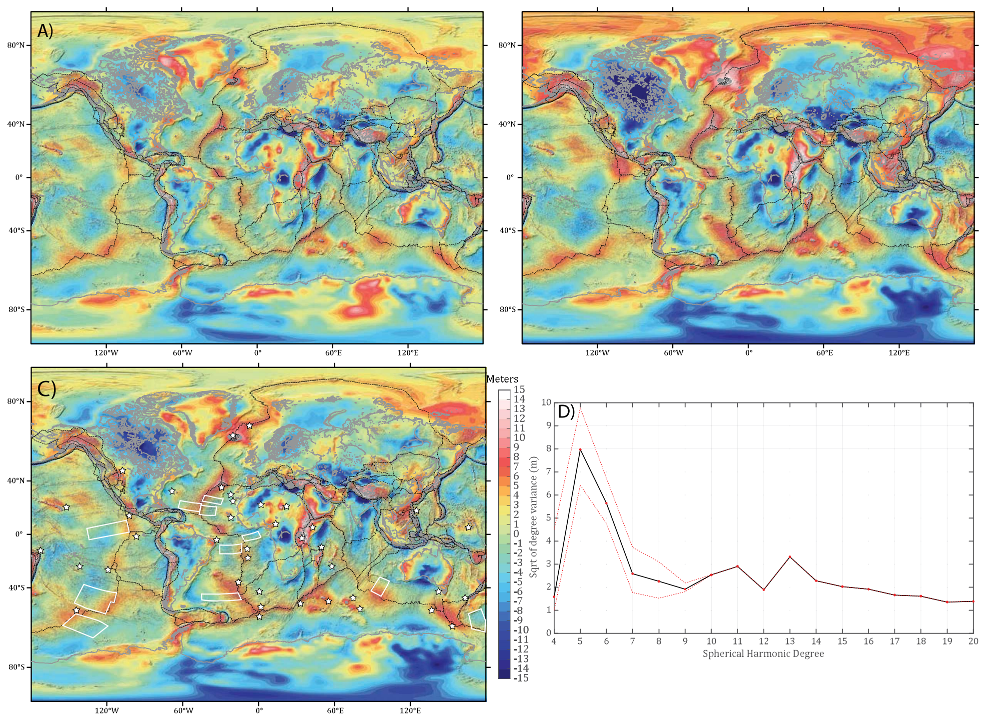

Figure 9. A-B) Lower and upper uncertainty bounds of UMG3. C) UGM3 model; white boxes denote the corridors of oceanic lithosphere used to obtain parameter β in Section 3. White stars indicate localities of prominent hotspots. D) Power spectra of UMG3 (black solid line) and its upper and lower uncertainty bounds (red dashed lines).

The major source of uncertainty in our modelling approach, and thus the only one considered here (as it overwhelms all other factors) is the calibration of parameter β in Eq. 6. This value was estimated based on the condition that peak-to-peak geoid variations along corridors of unperturbed oceanic lithosphere should remain close to those predicted by lithospheric cooling models. The fact that some additional cooling of the sublithospheric mantle can be expected to occur due to small-scale convection beneath the oceanic plate (e.g., Zlotnik et al., 2008; Afonso et al., 2008; Huang & Zhong, 2005) puts our estimates at the conservative end.

Considering all of the above, we apply a standard (linear) error propagation strategy (Morrison, 2021) to estimate confidence bounds for the power spectra and associated spatial patterns of the upper mantle residual geoid. The results, considered as conservative estimates, are shown in Fig. 9. The main difference between these maps is the absolute magnitude of the anomalies (although some changes in their relative magnitudes are also clear); their spatial patterns remain stable with respect to the underlying uncertainties. The effects of these uncertainties on estimates of the density-thermal structure of the lithosphere and sublithospheric upper mantle are beyond the scope of this paper, as they require multiple large-scale inversions. We therefore leave such an assessment for a future study.

5 Conclusions

We present a new upper mantle geoid model to inform studies of the physical state (temperature, composition, density) of the lithosphere and sublithospheric upper mantle. Rather than using pure spectral filtering, our model is based on the application of a 'direct approach', whereby the predicted geoid from a recent global model of density for depths > 400 km is removed from the total non-hydrostatic geoid. This preliminary residual upper mantle geoid is then analyzed and filtered in the spectral domain to remove remaining and spurious contributions from deep anomalies to obtain a representative geoid model of mantle densities above 400 km depth. We use this model and various spectral methods to i) constraint the hitherto unexplored contributions of upper mantle density anomalies to the low degrees ($4 < l < 8$) of spherical harmonic geoid expansions and ii) clarify the physical meaning of these density anomalies and their connection to the physical state of the upper mantle. In particular, we clarify the origin and strong contributions of the enigmatic degree 5, which is shown to be controlled by the interaction of global lithospheric structure and sublithospheric mantle flow.

Acknowledgments

We are indebted to A. Forte for providing the density model used in this study and for his insightful explanations and recommendations. FS and JCA acknowledge support from ARC Grant DP160103502, the ARC Centre of Excellence Core to Crust Fluids Systems (CCFS) and the Centre for Earth Evolution and Dynamics, Geoscience Australia and the European Space Agency via the "3D Earth - A Dynamic Living Planet". We used *m_map* package (Pawlowicz, R., 2020. "*M_Map*: A mapping package for MATLAB", version 1.4m, [Computer software], available online at www.eoas.ubc.ca/ rich/map.html) and MATLAB to plot all the figures in this study.

Open Research Section

The upper mantle geoid model (UMG3) discussed in this paper can be downloaded from: https://doi.org/10.6084/m9.figshare.21890775.v1.

References

Afonso, J. C., Salajegheh, F., Szwillus, W., Ebbing, J., & Gaina, C. (2019). A global reference model of the lithosphere and upper mantle from joint inversion and analysis of multiple data sets. *Geophysical Journal International*, *217*(3), 1602–1628.

Afonso, J. C., Zlotnik, S., & Fernandez, M. (2008). Effects of compositional and rheological stratifications on small-scale convection under the oceans: Implications for the thickness of oceanic lithosphere and seafloor flattening. *Geophysical Research Letters*, *35*(20).

Auer, L., Boschi, L., Becker, T., Nissen-Meyer, T., & Giardini, D. (2014). Savani: A variable resolution whole-mantle model of anisotropic shear velocity variations based on multiple data sets. *Journal of Geophysical Research: Solid Earth*, *119*(4), 3006–3034.

Becker, T. W., & Boschi, L. (2002). A comparison of tomographic and geodynamic mantle models. *Geochemistry, Geophysics, Geosystems*, *3*(1).

Bowin, C. (1983). Depth of principal mass anomalies contributing to the earth's geoidal undulations and gravity anomalies. *Marine Geodesy*, *7*(1-4), 61–100.

Bowin, C. (2000). Mass anomaly structure of the earth. *Reviews of Geophysics*, *38*(3), 355–387.

Bredow, E., Steinberger, B., Gassmöller, R., & Dannberg, J. (2022). Mantle convection and possible mantle plumes beneath antarctica–insights from geodynamic models and implications for topography. *Geological Society, London, Memoirs*, *56*(1), M56–2020.

Čadek, O., Yuen, D. A., & Čížková, H. (1998). Mantle viscosity inferred from geoid and seismic tomography by genetic algorithms: results for layered mantle flow. *Physics and Chemistry of the Earth*, *23*(9-10), 865–872.

Cazenave, A. (1995). Geoid, topography and distribution of landforms. *PDF). In Ahrens, Thomas J. Global earth physics a handbook of physical constants. Washington, DC: American Geophysical Union*.

Cazenave, A., Houry, S., Lago, B., & Dominh, K. (1992). Geosat-derived geoid anomalies at medium wavelength. *Journal of Geophysical Research: Solid Earth*, *97*(B5), 7081–7096.

Cazenave, A., Rosemberg-Borot, C., & Rabinowicz, M. (1986). Geoid lows over deep-sea trenches. *Journal of Geophysical Research: Solid Earth*, *91*(B2), 1989–2003.

Cazenave, A., Souriau, A., & Dominh, K. (1989). Global coupling of earth surface topography with hotspots, geoid and mantle heterogeneities. *Nature*, *340*(6228), 54–57.

Celli, N. L., Lebedev, S., Schaeffer, A. J., & Gaina, C. (2021). The tilted iceland plume and its effect on the north atlantic evolution and magmatism. *Earth and Planetary Science Letters*, *569*, 117048.

Chambat, F., Ricard, Y., & Valette, B. (2010). Flattening of the earth: further from hydrostaticity than previously estimated. *Geophysical Journal International*, *183*(2), 727–732.

Chase, C. (1985). The geological significance of the geoid. *Annual Review of Earth and Planetary Sciences*, *13*, 97.

Chase, C., Libarkin, J., & Sussman, A. (2002). Colorado plateau: Geoid and means of isostatic support. *International Geology Review*, *44*(7), 575–587.

Čížková, H., Čadek, O., Yuen, D. A., & Zhou, H.-w. (1996). Slope of the geoid spectrum and constraints on mantle viscosity stratification. *Geophysical research letters*, *23*(21), 3063–3066.

Coblentz, D., Chase, C., Karlstrom, K., & Van Wijk, J. (2011). Topography, the geoid, and compensation mechanisms for the southern rocky mountains. *Geochemistry, Geophysics, Geosystems*, *12*(4).

Coblentz, D., Van Wijk, J., Richardson, R. M., & Sandiford, M. (2015). The upper mantle geoid: Implications for continental structure and the intraplate stress field. *Geological Society of America Special Papers*, *514*, 197–214.
Davies, D. R., Valentine, A. P., Kramer, S. C., Rawlinson, N., Hoggard, M. J., Eakin, C. M., & Wilson, C. R. (2019, sep). Earth's multi-scale topographic response to global mantle flow. *Nature Geoscience 2019 12:10*, *12*(10), 845–850. Retrieved from https://www.nature.com/articles/s41561-019-0441-4 doi: 10.1038/s41561-019-0441-4
Delorey, A. A., Dunn, R. A., & Gaherty, J. B. (2007). Surface wave tomography of the upper mantle beneath the reykjanes ridge with implications for ridge–hot spot interaction. *Journal of Geophysical Research: Solid Earth*, *112*(B8). doi: 10.1029/2006JB004785
Doin, M., & Fleitout, L. (1996). Thermal evolution of the oceanic lithosphere: an alternative view. *Earth and Planetary Science Letters*, *142*(1), 121-136. Retrieved from https://www.sciencedirect.com/science/article/pii/0012821X96000829 doi: 10.1016/0012-821X(96)00082-9
Doin, M., Fleitout, L., & McKenzie, D. (1996). Geoid anomalies and the structure of continental and oceanic lithospheres. *Journal of Geophysical Research: Solid Earth*, *101*(B7), 16119–16135.
Featherstone, W. (1997). On the use of the geoid in geophysics: a case study over the north west shelf of australia. *Exploration Geophysics*, *28*(2), 52–57.
Fichtner, A., van Herwaarden, D.-P., Afanasiev, M., Simutė, S., Krischer, L., Çubuk-Sabuncu, Y., ... others (2018). The collaborative seismic earth model: generation 1. *Geophysical research letters*, *45*(9), 4007–4016.
Flament, N., Gurnis, M., & Müller, R. D. (2013). A review of observations and models of dynamic topography. *Lithosphere*, *5*(2), 189–210.
Fleitout, L., & Moriceau, C. (1992). Short-wavelength geoid, bathymetry and the convective pattern beneath the pacific ocean. *Geophysical Journal International*, *110*(1), 6–28.
Forte, A. M., Peltier, W., Dziewonski, A., & Woodward, R. (1993). Dynamic surface topography: A new interpretation based upon mantle flow models derived from seismic tomography. *Geophysical Research Letters*, *20*(3), 225–228.
Forte, A. M., Quéré, S., Moucha, R., Simmons, N. A., Grand, S. P., Mitrovica, J. X., & Rowley, D. B. (2010). Joint seismic–geodynamic-mineral physical modelling of african geodynamics: A reconciliation of deep-mantle convection with surface geophysical constraints. *Earth and Planetary Science Letters*, *295*(3-4), 329–341.
French, S., & Romanowicz, B. A. (2014). Whole-mantle radially anisotropic shear velocity structure from spectral-element waveform tomography. *Geophysical Journal International*, *199*(3), 1303–1327.
Fullea, J., Lebedev, S., Martinec, Z., & Celli, N. (2021). Winterc-g: mapping the upper mantle thermochemical heterogeneity from coupled geophysical–petrological inversion of seismic waveforms, heat flow, surface elevation and gravity satellite data. *Geophysical Journal International*, *226*(1), 146–191.
Golle, O., Dumoulin, C., Choblet, G., & Cadek, O. (2012). Topography and geoid induced by a convecting mantle beneath an elastic lithosphere. *Geophysical Journal International*, *189*(1), 55–72.
Hager, B. (1984). Subducted slabs and the geoid: Constraints on mantle rheology and flow. *Journal of Geophysical Research: Solid Earth*, *89*(B7), 6003–6015.
Hager, B., Clayton, R. W., Richards, M. A., Comer, R. P., & Dziewonski, A. M. (1985). Lower mantle heterogeneity, dynamic topography and the geoid. *Nature*, *313*(6003), 541–545.
Hager, B., & Richards, M. (1989). Long-wavelength variations in earth's geoid: physical models and dynamical implications. *Philosophical Transactions of the Royal Society of London. Series A, Mathematical and Physical Sciences*,

328 (1599), 309–327.

Haxby, W. F., & Turcotte, D. L. (1978). On isostatic geoid anomalies. *Journal of Geophysical Research: Solid Earth*, *83* (B11), 5473-5478. doi: 10.1029/JB083iB11p05473

Hoggard, M. J., White, N., & Al-Attar, D. (2016, may). Global dynamic topography observations reveal limited influence of large-scale mantle flow. *Nature Geoscience 2016 9:6*, *9* (6), 456–463. Retrieved from `https://www.nature.com/articles/ngeo2709` doi: 10.1038/ngeo2709

Huang, J., & Zhong, S. (2005). Sublithospheric small-scale convection and its implications for the residual topography at old ocean basins and the plate model. *Journal of Geophysical Research: Solid Earth*, *110* (B5).

Ji, F., Zhang, Q., Xu, M., Zhou, X., & Guan, Q. (2021). Estimating the effective elastic thickness of the arctic lithosphere using the wavelet coherence method: Tectonic implications. *Physics of the Earth and Planetary Interiors*, *318*, 106770.

Jordan, T. H. (1978). Composition and development of the continental tectosphere. *Nature*, *274* (5671), 544–548.

Kaula, W. M. (1967). Geophysical implications of satellite determinations of the earth's gravitational field. *Space Science Reviews*, *7* (5), 769–794.

Kido, M., Yuen, D. A., Čadek, O., & Nakakuki, T. (1998). Mantle viscosity derived by genetic algorithm using oceanic geoid and seismic tomography for whole-mantle versus blocked-flow situations. *Physics of the Earth and Planetary Interiors*, *107* (4), 307–326.

Lambeck, K. (1976). Lateral density anomalies in the upper mantle. *Journal of Geophysical Research*, *81* (35), 6333–6340.

Lambeck, K. (1979, apr). Methods and geophysical applications of satellite geodesy. *Reports on Progress in Physics*, *42* (4), 547. doi: 10.1088/0034-4885/42/4/001

Le Stunff, Y., & Ricard, Y. (1995, dec). Topography and geoid due to lithospheric mass anomalies. *Geophysical Journal International*, *122* (3), 982–990. Retrieved from `https://academic.oup.com/gji/article/122/3/982/720603` doi: 10.1111/J.1365-246X.1995.TB06850.X

Lebedeva-Ivanova, N., Gaina, C., Minakov, A., & Kashubin, S. (2019). Arccrust: Arctic crustal thickness from 3-d gravity inversion. *Geochemistry, Geophysics, Geosystems*, *20* (7), 3225–3247.

Liu, X., & Zhong, S. (2015). The long-wavelength geoid from three-dimensional spherical models of thermal and thermochemical mantle convection. *Journal of Geophysical Research: Solid Earth*, *120* (6), 4572–4596.

Liu, X., & Zhong, S. (2016). Constraining mantle viscosity structure for a thermochemical mantle using the geoid observation. *Geochemistry, Geophysics, Geosystems*, *17* (3), 895–913.

Lu, C., Forte, A. M., Simmons, N. A., Grand, S. P., Kajan, M. N., Lai, H., & Garnero, E. J. (2020). The sensitivity of joint inversions of seismic and geodynamic data to mantle viscosity. *Geochemistry, Geophysics, Geosystems*, *21* (4), e2019GC008648.

Marks, K. M., Sandwell, D., Vogt, P. R., & Hall, S. A. (1991). Mantle downwelling beneath the australian-antarctic discordance zone: Evidence from geoid height versus topography. *Earth and Planetary Science Letters*, *103* (1-4), 325–338.

Marquart, G. (1991). Finite element modeling of lower crustal flow: A model for crustal thickness variations. *Journal of Geophysical Research: Solid Earth*, *96* (B12), 20331-20335. doi: 10.1029/91JB01887

McKenzie, D. (1966). The viscosity of the lower mantle. *Journal of Geophysical Research (1896-1977)*, *71* (16), 3995-4010. doi: 10.1029/JZ071i016p03995

McKenzie, D., Watts, A., Parsons, B., & Roufosse, M. (1980). Planform of mantle convection beneath the pacific ocean. *Nature*, *288* (5790), 442–446.

Minakov, A., & Gaina, C. (2021). Probabilistic linear inversion of satellite gravity gradient data applied to the northeast atlantic. *Journal of Geophysical Research (JGR): Solid Earth*, *126*(12).

Morrison, F. A. (2021). *Uncertainty analysis for engineers and scientists: A practical guide*. Cambridge University Press.

Moucha, R., Forte, A. M., Mitrovica, J. X., Rowley, D. B., Quéré, S., Simmons, N. A., & Grand, S. P. (2008). Dynamic topography and long-term sea-level variations: There is no such thing as a stable continental platform. *Earth and Planetary Science Letters*, *271*(1-4), 101–108.

Nakiboglu, S. (1982). Hydrostatic theory of the earth and its mechanical implications. *Physics of the Earth and Planetary Interiors*, *28*(4), 302–311.

O'Connell, R. J. (1971). Pleistocene glaciation and the viscosity of the lower mantle. *Geophysical Journal International*, *23*(3), 299–327.

O'Donnell, J., Daly, E., Tiberi, C., Bastow, I., O'Reilly, B., Readman, P., & Hauser, F. (2011). Lithosphere-asthenosphere interaction beneath ireland from joint inversion of teleseismic p-wave delay times and grace gravity. *Geophysical Journal International*, *184*(3), 1379–1396.

Panasyuk, S. V., & Hager, B. (2000a). Inversion for mantle viscosity profiles constrained by dynamic topography and the geoid, and their estimated errors. *Geophysical Journal International*, *143*(3), 821–836.

Panasyuk, S. V., & Hager, B. (2000b). Models of isostatic and dynamic topography, geoid anomalies, and their uncertainties. *Journal of Geophysical Research: Solid Earth*, *105*(B12), 28199–28209.

Panning, M., & Romanowicz, B. (2006). A three-dimensional radially anisotropic model of shear velocity in the whole mantle. *Geophysical Journal International*, *167*(1), 361–379.

Pasyanos, M. E., Masters, T. G., Laske, G., & Ma, Z. (2014). Litho1. 0: An updated crust and lithospheric model of the earth. *Journal of Geophysical Research: Solid Earth*, *119*(3), 2153–2173.

Pavlis, N. K., Holmes, S. A., Kenyon, S. C., & Factor, J. K. (2012). The development and evaluation of the earth gravitational model 2008 (egm2008). *Journal of geophysical research: solid earth*, *117*(B4).

Pease, V., Drachev, S., Stephenson, R., & Zhang, X. (2014). Arctic lithosphere—a review. *Tectonophysics*, *628*, 1–25.

Perrot, K., Tarits, P., & Goslin, J. (1997). Regionalized comparison of global earth models of seismic velocity, geoid and topography: implications on the geodynamics of ridges and subductions. *Physics of the earth and planetary interiors*, *99*(1-2), 91–102.

Rapp, R. (1973). Geoid information by wavelength. *Bulletin Géodésique (1946-1975)*, *110*(1), 405–411.

Rapp, R. (1982a). Degree variances of the earth's potential, topography and its isostatic compensation. *Bulletin géodésique*, *56*(2), 84–94.

Rapp, R. (1982b). A global atlas of sea surface heights based on seasat altimeter data. *Reports of the Department of Geodetic Science and Surveying*(333).

Ricard, Y., Vigny, C., & Froidevaux, C. (1989). Mantle heterogeneities, geoid, and plate motion: A monte carlo inversion. *Journal of Geophysical Research: Solid Earth*, *94*(B10), 13739–13754.

Richards, M. A., & Hager, B. (1984). Geoid anomalies in a dynamic earth. *Journal of Geophysical Research: Solid Earth*, *89*(B7), 5987–6002.

Richards, M. A., Hager, B., & Sleep, N. H. (1988). Dynamically supported geoid highs over hotspots: Observation and theory. *Journal of Geophysical Research: Solid Earth*, *93*(B7), 7690–7708.

Rong-Shan, F. (1989). Plate motions, earth's geoid anomalies, and mantle convection. *Slow Deformation and Transmission of Stress in the Earth*, *49*, 47–54.

Rowley, D. B., Forte, A. M., Moucha, R., Mitrovica, J. X., Simmons, N. A., & Grand, S. P. (2013). Dynamic topography change of the eastern united states since 3 million years ago. *science*, *340*(6140), 1560–1563.

Rowley, D. B., Forte, A. M., Rowan, C. J., Glišović, P., Moucha, R., Grand, S. P., & Simmons, N. A. (2016). Kinematics and dynamics of the east pacific rise linked to a stable, deep-mantle upwelling. *Science advances*, *2*(12), e1601107.

Sandwell, D. (2022). *Advanced geodynamics*. Cambridge University Press.

Sandwell, D., & Schubert, G. (1980). Geoid height versus age for symmetric spreading ridges. *Journal of Geophysical Research: Solid Earth*, *85*(B12), 7235-7241. doi: 10.1029/JB085iB12p07235

Schaeffer, A., & Lebedev, S. (2013). Global shear speed structure of the upper mantle and transition zone. *Geophysical Journal International*, *194*(1), 417–449.

Schubert, G. (2015). *Treatise on geophysics*. Elsevier.

Simmons, N. A., Forte, A. M., Boschi, L., & Grand, S. P. (2010). Gypsum: A joint tomographic model of mantle density and seismic wave speeds. *Journal of Geophysical Research: Solid Earth*, *115*(B12).

Toksöz, M. N., Arkani-Hamed, J., & Knight, C. A. (1969). Geophysical data and long-wave heterogeneities of the earth's mantle. *Journal of Geophysical Research (1896-1977)*, *74*(15), 3751-3770. doi: 10.1029/JB074i015p03751

Van Camp, M. J., de Viron, O., & Ferreira, A. (2019). Comparing global seismic tomography models using the varimax principal component analysis. In *Agu fall meeting abstracts* (Vol. 2019, pp. S23F–0705).

Vening Meinesz, F. (1951). A remarkable feature of the earth's topography. In *Proc. k. ned. akad. wet. ser. b phys. sci* (Vol. 54, pp. 212–228).

Wang, H., Wu, P., & Wang, Z. (2006). An approach for spherical harmonic analysis of non-smooth data. *Computers & geosciences*, *32*(10), 1654–1668.

Wieczorek, M. (2007). 10.05 - gravity and topography of the terrestrial planets. In G. Schubert (Ed.), *Treatise on geophysics* (p. 165-206). Amsterdam: Elsevier.

Zhang, J.-J., Zheng, Y.-F., & Zhao, Z.-F. (2009). Geochemical evidence for interaction between oceanic crust and lithospheric mantle in the origin of cenozoic continental basalts in east-central china. *Lithos*, *110*(1), 305-326. Retrieved from `https://www.sciencedirect.com/science/article/pii/S0024493709000279` doi: 10.1016/j.lithos.2009.01.006

Zlotnik, S., Afonso, J. C., Díez, P., & Fernández, M. (2008). Small-scale gravitational instabilities under the oceans: Implications for the evolution of oceanic lithosphere and its expression in geophysical observables. *Philosophical magazine*, *88*(28-29), 3197–3217.

Supporting Information for "The upper mantle geoid for lithospheric structure and dynamics"

F. Salajegheh[1], J.C. Afonso[2,3,1]

[1]Department of Earth and Environmental Sciences, Macquarie University, Sydney, Australia.
[2]Faculty of Geo-Information Science and Earth Observation (ITC), University of Twente, Enschede, Netherlands.
[3]Department of Earth and Space Sciences, Southern University of Science and Technology Shenzhen, Guangdong, China

Content of this file

Figures S1 to S8

Introduction

This supporting information provides eight figures referred to in the original text (Figure S1 to Figures S8).

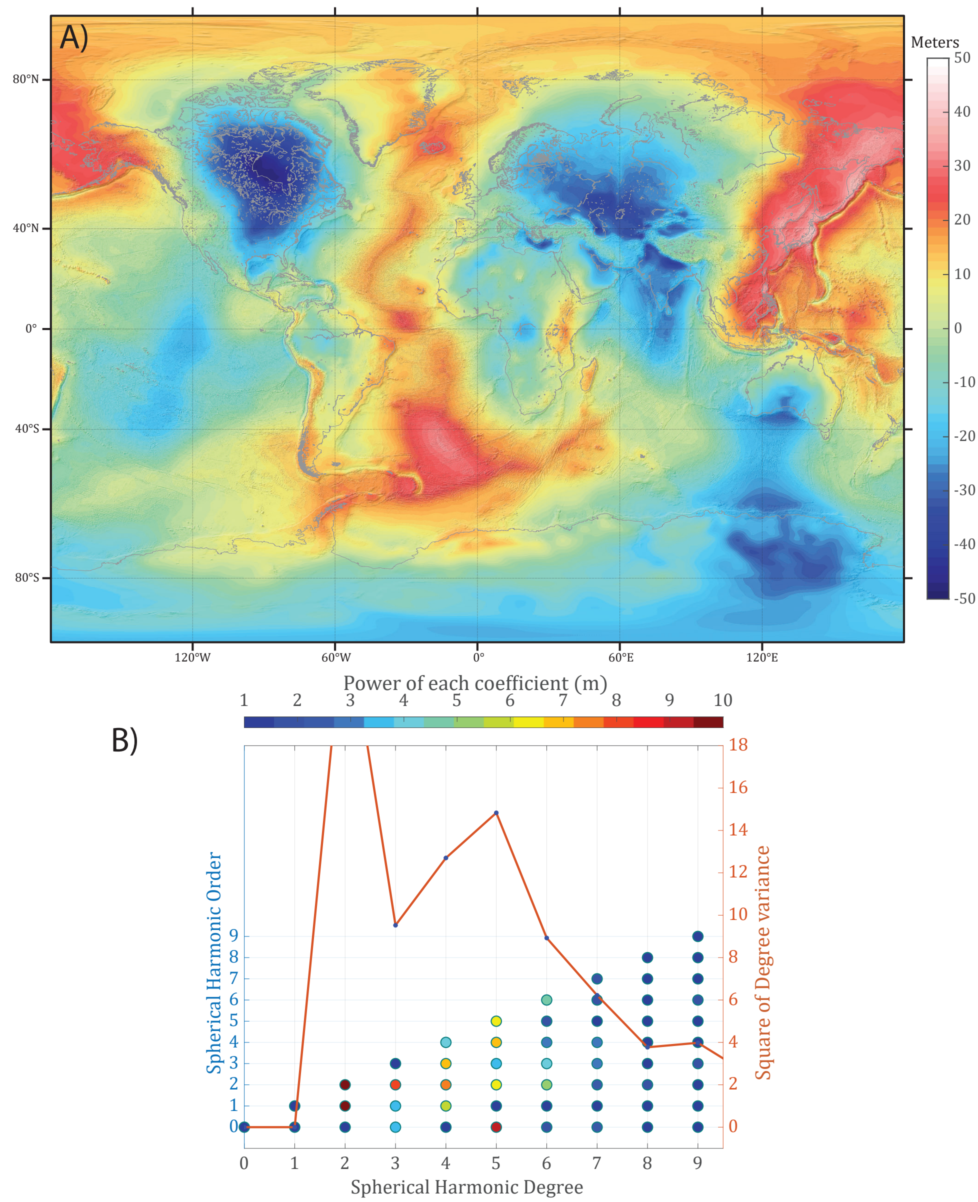

Figure S1. A) UMG1, the preliminary residual geoid by subtracting the SGM20 'lower mantle' contribution from the full, observed non-hydrostatic geoid. B) Power spectrum of the residual geoid (UMG1) with the contribution to the power from each order and degree. The left vertical axis refers to the spherical harmonic order, the horizontal axis to the degree of the coefficients. The red line is square of degree variance of UMG1

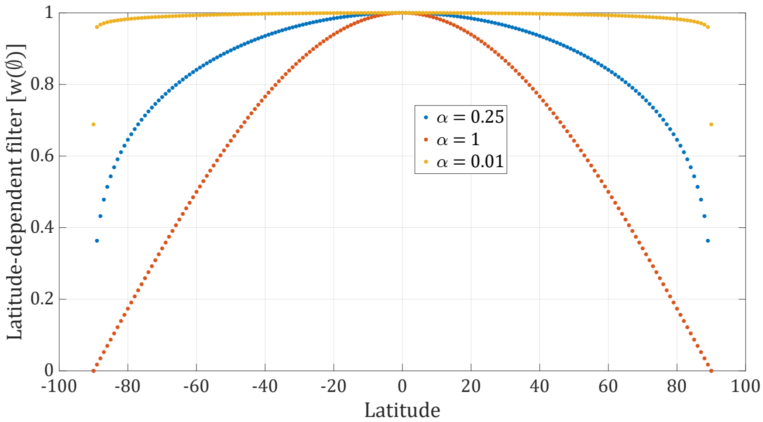

Figure S2. Effect of α on the latitude-dependent weighting factor (see main text). Higher values of α produce a more rapid decay of the orders 2-3 with latitude.

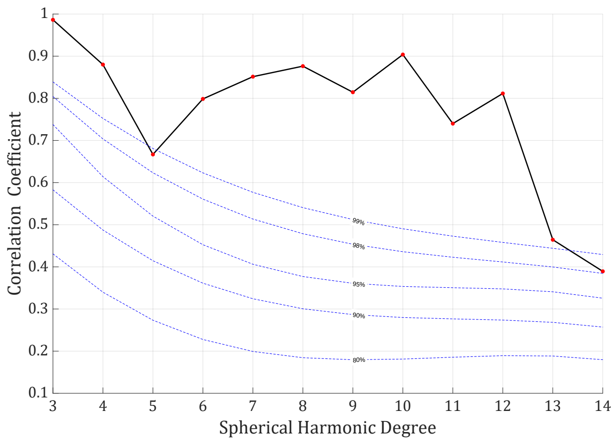

Figure S3. Degree correlation between the the full non-hydrostatic geoid and the lower mantle component from the SGM20 model ($D_l(geoid, SGM20)$)

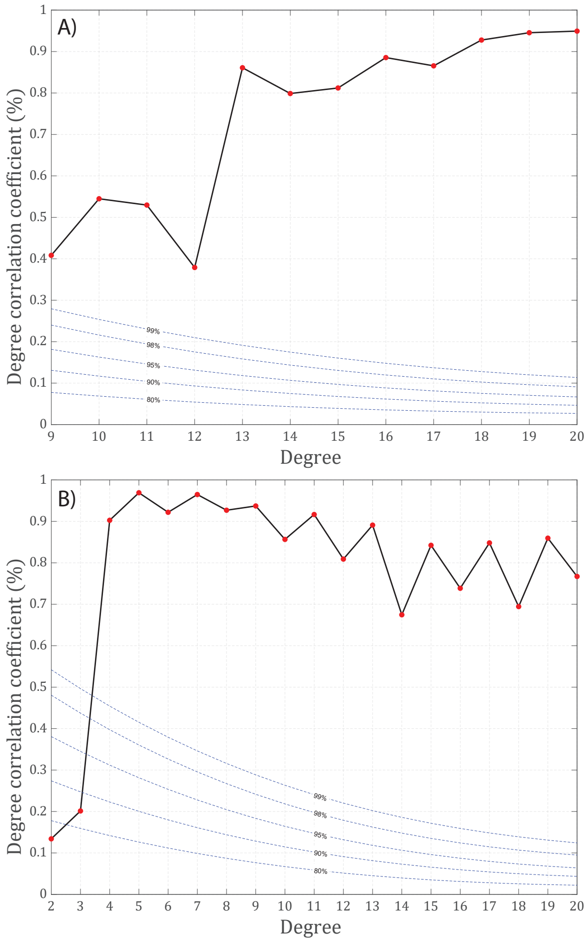

Figure S4. Degree correlation coefficients per degree between the full non-hydrostatic geoid and the predicted geoid from two upper mantle density models: A) $LithoRef18$ (Afonso et al., 2019), B) WINTREC Fullea et al. (2021).

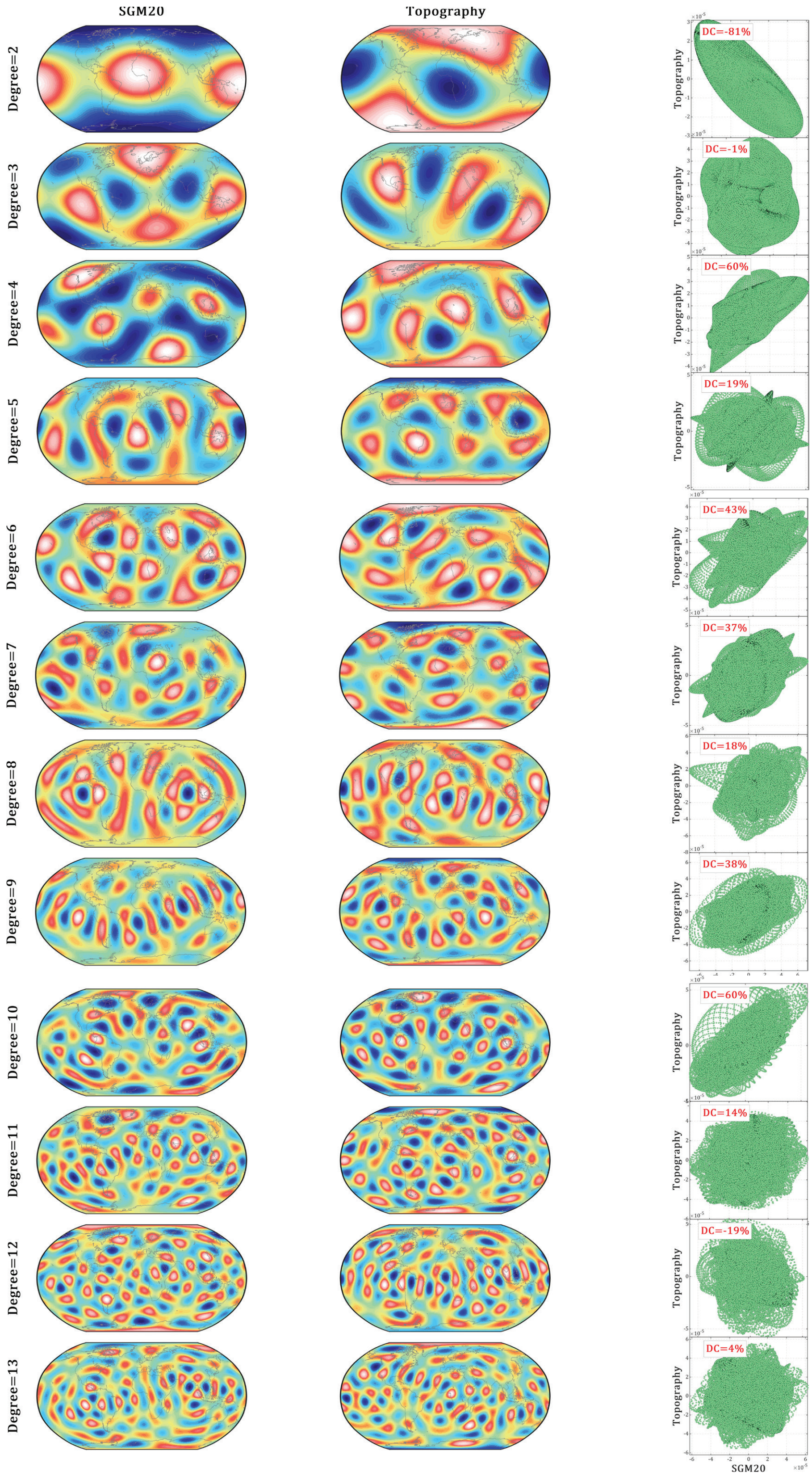

Figure S5. Maps of individual contributions from each degree for the lower mantle component of the SGM20 model (first column) and global topography (second column). The last column shows the degree correlation plots between the maps in the first and second columns. Each panel includes the degree correlation value (red text).

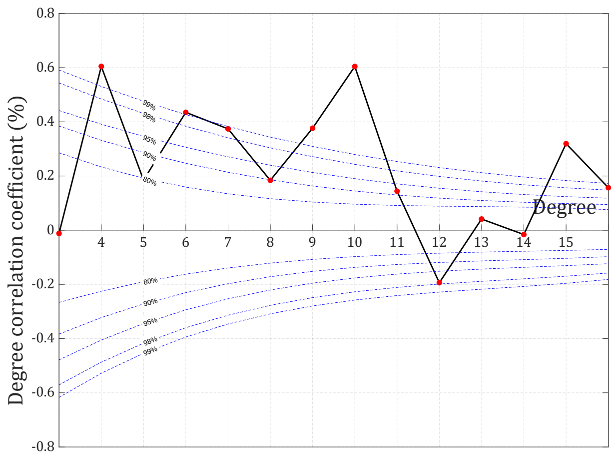

Figure S6. Degree correlation between global topography and the lower mantle component of the SGM20 model.

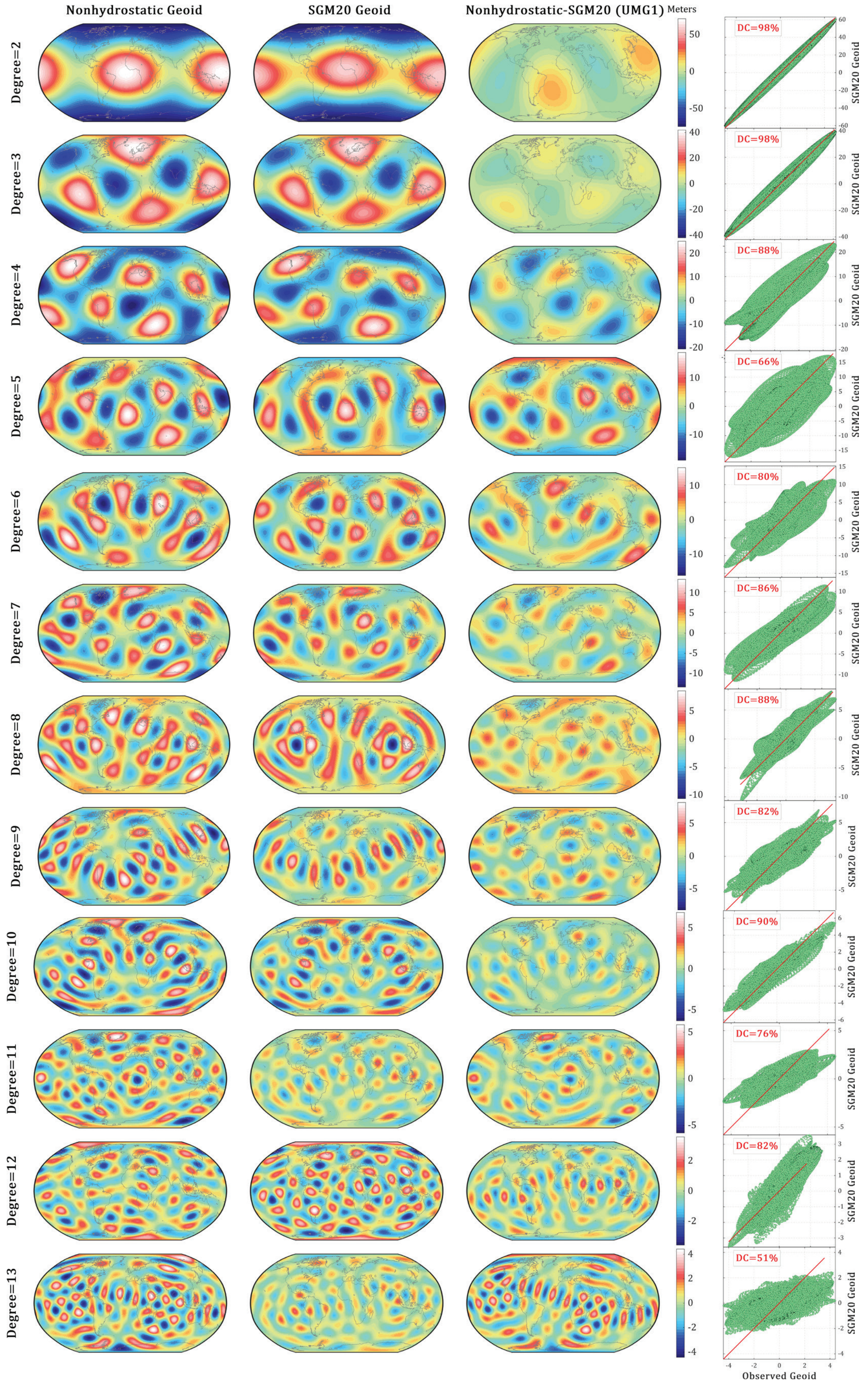

Figure S7. Maps of individual contributions from each degree for the full non-hydrostatic geoid (first column), the lower mantle component of the SGM20 model (second column) and their difference (UMG1, third column). The last column shows the degree correlation plots between the maps in the first and second columns. Each panel includes the degree correlation value (red text).

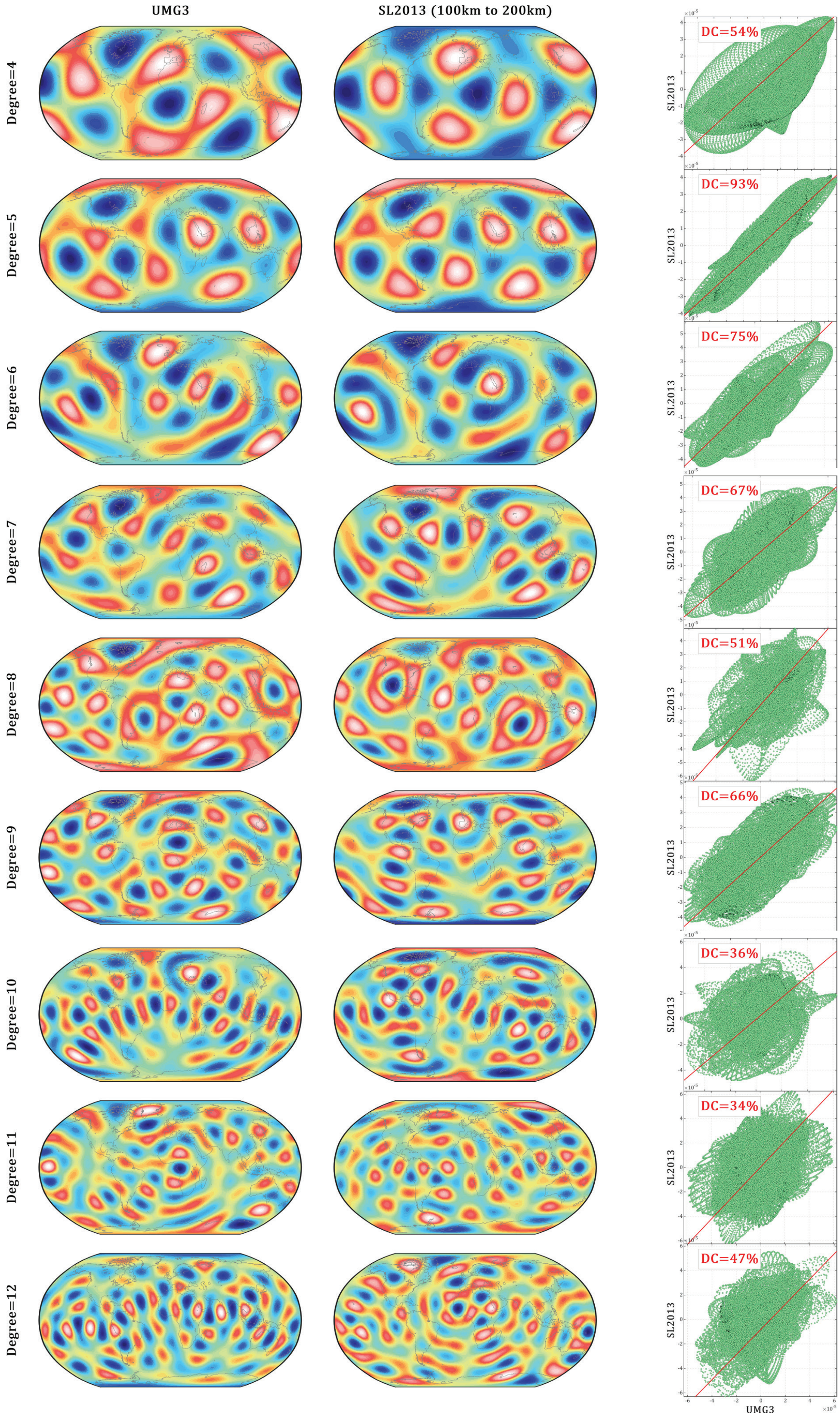

Figure S8. Maps of individual contributions from each degree for UMG3 (first column) and SL2013 (second column); for the latter we use the average velocity in the depth range 100-200 km. The last column shows the degree correlation plots between the maps in the first and second columns. Each panel includes the degree correlation value (red text).

References

Afonso, J. C., Salajegheh, F., Szwillus, W., Ebbing, J., & Gaina, C. (2019). A global reference model of the lithosphere and upper mantle from joint inversion and analysis of multiple data sets. *Geophysical Journal International*, *217*(3), 1602–1628.

Fullea, J., Lebedev, S., Martinec, Z., & Celli, N. (2021). Winterc-g: mapping the upper mantle thermochemical heterogeneity from coupled geophysical–petrological inversion of seismic waveforms, heat flow, surface elevation and gravity satellite data. *Geophysical Journal International*, *226*(1), 146–191.